General Disclaimer

One or more of the Following Statements may affect this Document

- This document has been reproduced from the best copy furnished by the organizational source. It is being released in the interest of making available as much information as possible.

- This document may contain data, which exceeds the sheet parameters. It was furnished in this condition by the organizational source and is the best copy available.

- This document may contain tone-on-tone or color graphs, charts and/or pictures, which have been reproduced in black and white.

- This document is paginated as submitted by the original source.

- Portions of this document are not fully legible due to the historical nature of some of the material. However, it is the best reproduction available from the original submission.

Produced by the NASA Center for Aerospace Information (CASI)

Cornell → NGL-33-010-082
Columbia → NGR-33-008-012

NEAR INFRARED LIGHT SCATTERING BY TERRESTRIAL CLOUDS

James E. Hansen
Goddard Space Flight Center
Institute for Space Studies, NASA
New York, New York

James B. Pollack
Laboratory for Planetary Studies
Center for Radiophysics and Space Research
Cornell University
Ithaca, New York

RECEIVED MAR 1970 NASA STI FACILITY INPUT BRANCH

N70-20854 (ACCESSION NUMBER) (THRU)
63 (PAGES) 1 (CODE)
TMX#62818 (NASA CR OR TMX OR AD NUMBER) 20 (CATEGORY)
FORM 602

1. Introduction

Sagan and Pollack (1967), Pollack and Sagan (1968), and Hansen and Cheyney (1968, 1969) have pointed out that some physical properties of clouds, such as mean particle size and optical depth, can be inferred from an analysis of the clouds' near infrared reflectivity. Below we analyze observations of terrestrial water and ice clouds with this expectation in mind. It affords us an opportunity both to deduce the properties of these clouds and to check the consistency of our approach when applied to clouds we know something about. It is especially important to obtain tests of the plane-parallel approximation for real atmospheric cloud systems and the Mie scattering approximation for ice crystals.

After outlining our computational scheme, we summarize the theoretical results for single scattering. These illustrate the effects on the scattering of various input parameters. Subsequently we discuss the infrared observations of Blau, et al. and attempt to remove the effects of gaseous absorption. In the next section we summarize the absorption corrections and relate them to the clouds' temperature and to the mode of line formation. Finally, we estimate the phase, mean particle size, and optical depth of selected clouds from their spectral and angular scattering behavior.

2. Computational method

To obtain the spectral reflectivity of clouds and the angular distribution of the scattered light we first computed the single scattering from a small volume containing a representative distribution of particle sizes and then the multiple scattering for the entire cloud. The single scattering computations were made using the Mie theory in essentially the way described by Deirmendjian and Clasen (1962). However, the logarithmic derivatives of certain spherical Bessel functions occurring in the series were obtained by proceeding from the highest order terms; Kattawar and Plass (1967) have pointed out that an upward progression for the recursion relations is basically unstable and may cause significant errors for large size parameters. The validity of our single scattering solutions was checked by making comparisons to published results of Deirmendjian (1964), unpublished company reports by the same author and unpublished work of H. Cheyney.

We employed Deirmendjian's (1964) "Cloud model" for the distribution of particle sizes,

$$n(r) \propto r^6 \exp(-6r/r_m) \qquad (1)$$

where n(r) is the volume concentration of radius r and r_m is the radius at which the distribution has its maximum. Although sample size distributions from actual clouds often differ markedly from Deirmendjian's model, it serves the purpose of averaging out most of the large fluctuations which occur in the phase function (scattering diagram) for a single sphere. We have made preliminary computations to find the effect of changing the shape of the size distribution; the results for several different distributions indicate that the volume extinction (σ_{ext}) the single scattering albedo (ω), the asymmetry factor ($\langle \cos \theta \rangle$) and the shape of the phase function (outside the region of the glory) depend mainly on the mean particle radius for extinction,

$$\bar{r} = \frac{\int_0^\infty \sigma_{ext}(r)\, n(r) r dr}{\int_0^\infty \sigma_{ext}(r)\, n(r)\, dr}, \qquad (2)$$

and not on the shape of the size distribution. This indicates that our computations in this paper with a single type of size distribution are meaningful, although in cases where

a more exact knowledge of the size distribution is available it should of course be used. For this paper our computations were made with r_m = 2, 4, 8, 16 and 32μ with the integrations over particle size extended to the radius r_{max} = 25μ for the first four distributions and to r_{max} = 50μ for the case r_m = 32μ. The integration increments were chosen small enough to make the phase function smooth (see, e.g., Dave, 1969a, 1969b). The values used for r_{max} were somewhat arbitrary but that is not essential since the purpose of the integration over particle sizes was to smooth out single particle effects; we usually found $\overline{r} \simeq r_m$.

Except where otherwise indicated we employed the optical constants for water and ice tabulated by Irvine and Pollack (1968); the computations were made at each wavelength ($\sim$ 50) at which the authors tabulate the optical constants for the region of interest ($1.2 \geq \lambda \geq 3.6\mu$).

The intensity of light multiply scattered by the clouds was obtained by using the "double only" computing method, described by Hansen (1969a), which is a variation of van de Hulst's (1963) doubling method. If errors $\leqslant$ 1% are tolerable, as is certainly the case for comparison to most observations, then the computing time may be greatly speeded up. Some of the more useful shortcuts which we have tested are described in the appendix.

3. Results for single scattering

The single scattering behavior of an ensemble of aerosols is a function of the complex index of refraction, $n_c = n_r - in_i$, and the distribution of particle sizes, expressed in units of the ratio of the circumference of the particle to the wavelength λ: $x = 2\pi r/\lambda$. Assuming that the distribution of size is given by (1), we find that the parameter x_m, which equals $2\pi r_m/\lambda$, serves to define the dependence of the scattering behavior upon particle size. The results described below are of both general interest and of help in understanding the infrared properties of terrestrial clouds analyzed in later sections. In the calculations for Figs. 1-3 the integrations over the size parameter x were performed to an upper limit of $x_{max} = 2x_m$, except when $x_m = 128$ for which x_{max} was set equal to 200.

a. General single scattering results

Fig. 1 shows the dependence of the normalized phase function $p(\theta)$ (Deirmendjian, 1964, 1969) upon the particle size parameter x_m in the case of no absorption ($n_i = 0$) with the real refractive index equal to 1.33, the value for liquid water

in the visible. The variable θ is the angle of scatter.

The individual curves have been vertically displaced from one another. The short horizontal line intersecting a given phase curve denotes the position at which the phase function has a value of unity. For the largest values of x_m, the very precipitous decline in the value of p near 0° corresponds to the diffraction peak (Deirmendjian, 1964, Dave, 1969c); the strong maximum at a scattering angle of 142° is the main rainbow (caused by rays undergoing a single internal reflection) with its first supernumery bow (van de Hulst, 1957, p. 241) located at 147°; the second rainbow (2 internal reflections) is located at 123° while its first supernumery bow lies at 114°; and finally the glory corresponds to the overall increase and oscillatory behavior near 180°. As x_m decreases all these features become less pronounced and broader; in addition the rainbow shifts in location towards larger scattering angles and the slope of the phase function decreases until near $x_m = 1/2$ it is very similar to the Rayleigh phase function.

The effect of introducing absorption within the particles is investigated in Fig. 2. For $x_m = 32$, the glory and rainbow have been effectively suppressed when n_i is comparable to or larger than 0.03. This effect can be understood using concepts from geometrical optics. A ray traversing a path equal to the particle radius will be diminished in strength by $\exp(-ka) = \exp(-2 x n_i)$ where k is the linear absorption coefficient. Setting n_i equal to 0.03 and x to 32, we see that the ray is diminished by almost a factor of 10 in intensity. Similarly the diffraction component which is not affected by absorption, extends to larger scattering angles as n_i increases.

For x_m again of 32, the value of the phase function in the backward hemisphere ($\theta > 90^o$) begins to increase as n_i becomes larger than 0.1. This may be attributed to an enhanced value of externally reflected light, as seen from the Fresnel equation. For the smaller particles ($x_m = 2$) the results are basically similar, although less pronounced.

Finally we study the influence of the real part of the index of refraction in Fig. 3. For $x_m = 32$, increasing n_r causes the rainbow to shift to larger scattering angles, until it merges with the glory, resulting in a large increase in p (180°). Aside from the diffraction peak, small angle scattering becomes more dominant as the refractive index decreases, a result which shows up in the asymmetry factor $< \cos \theta >$ described below. We will find this effect to

be of significance in understanding certain spectral characteristics of water clouds. Similarly at the lower values of n_r refraction tends to dominate over diffraction at smaller angles of incidence and hence the break in the diffraction peak occurs at smaller values of θ. The right hand half of the figure shows that similar effects occur for particles with absorption ($n_i = 0.01$) and small particles ($x_m = 2$).

b. Single scattering for water and ice

One important integral scattering parameter is the single scattering albedo, $\tilde{\omega}$, the ratio of the amount of light scattered to that which is scattered and absorbed. In Figs. 4 and 5 the spectral variation of $1 - \tilde{\omega}$ is exhibited for liquid water and ice particles, respectively, for five values of the size parameter r_m.

As noted by Irvine and Pollack (1968), the maxima and minima of ice and water are displaced by about 0.1μ in wavelength, a feature useful in distinguishing the phase of water clouds. Also the single scattering albedo generally declines monotonically with increasing particle size. It should be noted that in all cases $x_m > 3$. For sizes much smaller than this the particles will become completely absorbing and the above generalization is no longer true (van de Hulst, 1957). An interesting mild deviation from the general variation of $\tilde{\omega}$ with particle size occurs near a wavelength of 3μ and may be due to the perturbing effect of the smallest particles having values of $x < 1$. Near 3μ the value of n_i is so large that the particles become completely opaque so that allowing

for the diffraction peak $\tilde{\omega}$ is about 1/2.

The asymmetry factor $\langle \cos \theta \rangle$ is defined as the solid angle average of $\cos \theta$ weighted by the phase function. It describes the degree of forward scattering of the phase function. For isotropic scattering it has a value of zero while it approaches unity as small angle scattering tends to dominate. Figs. 6 and 7 show the spectral behavior of $\langle \cos \theta \rangle$ for liquid water and ice particles, respectively. For the largest value of x_m there is a very pronounced increase in $\langle \cos \theta \rangle$ slightly shortward of 3μ and a less obvious minimum somewhat longward of 3μ. This behavior reflects the anamolous despersion changes in n_r near the very strong absorption feature centered near 3μ, with changes in n_i also influencing $\langle \cos \theta \rangle$ near its minima. As shown in Fig. 3 and discussed earlier the phase function becomes more forward scattering as n_r approaches unity.

From multiple scattering computations reported below and elsewhere (Hansen, 1969a; Hansen and Cheyney, 1968) we find that for wavelengths less than 2.5μ and between 3.4 and 3.6μ the reflectivity of thick clouds depends primarily on the single scattering albedo, qualitatively the curves of $\log (1 - \tilde{\omega})$ are very similar to the spectral variation of the cloud reflectivities. As the single scattering albedo decreases, the less probable it is for a photon to survive a number of scattering events. Since the single scattering

albedo in these wavelength regions varies systematically with the characteristic particle size r_m (cf. Figs. 4 and 5) we can obtain particle size information from the near infrared spectral behavior of clouds, as has been pointed out by Sagan and Pollack (1967), Hansen and Cheyney (1968), and Irvine and Pollack (1968).

On the other hand in the spectral region between 2.5 and 3.4μ the single scattering albedo has a constant value of about 1/2 and the spectral behavior of the cloud reflectivity depends primarily on $\langle \cos \theta \rangle$. There is an inverse qualitative similarity between the wavelength variation of $\langle \cos \theta \rangle$ and computed cloud reflectivities. As $\langle \cos \theta \rangle$ increases, less light incident on a cloud layer is reflected back out in the first few scattering events. If the single scattering albedo is sufficiently less than one so that these scattering events are the major producers of reflected photons, the cloud reflectivity will decrease as $\langle \cos \theta \rangle$ increases. For example the maximum in $\langle \cos \theta \rangle$ slightly shortward of 3μ results in a minimum value for the cloud reflectivity at the same wavelength, as shown below. The spectral variation of $\langle \cos \theta \rangle$ is a reflection of the spectral behavior of the indices of refraction.

4. Reflectivity measurements of terrestrial clouds

Blau, Espinola, and Reifenstein (1966; see Blau and Espinola, 1965, for a more detailed report) have obtained airborne infrared measurements of the reflectance properties of terrestrial clouds. These consist of both spectral and angular observations. Observations were perfomed from an aircraft above the cloud of interest and on a given day measurements were made either in the 1.2μ to 2.5μ region or the 2.4μ to 3.6μ wavelength domain. In addition on some occasions angular scattering information was obtained by flying along a hexagonal path and performing spectral measurements of the cloud area situated at the center of the hexagon. In such measurements the angles of reflection and incidence remain constant, while the azimuth and angle of scatter vary. Below we describe these observations in greater detail and outline the transformation we applied to them so as to be able to compare them with our multiple scattering computations.

The spectral radiance (specific intensity) I_λ values reported by Blau et al. refer to averages of a number of spectra obtained close together in time. In addition they also give values for the standard deviation of each average value. The standard deviation is not necessarily a reflection of the error of measurement, because it also includes short term variations in the properties of the observed cloud.

We subjected these measurements to two types of transformations. First we divided the observed specific intensity by the solar flux outside the atmosphere of the earth, F_λ:

$$R_\lambda = \frac{I_\lambda}{\mu_o \; F_{\lambda/\pi}} = \frac{S}{4\mu \; \mu_o} \qquad (3)$$

where S, defined by Eq. (3), is the usual scattering function, $\theta_o = \cos^{-1}\mu_o$ the angle of incidence, and $\theta = \cos^{-1}\mu$ the angle of reflection. If the clouds were a lambert surface, i.e., if they scattered isotropically, the normalized reflectivity R_λ would equal the spherical albedo of the clouds and would exhibit no angular variation.

All the spectra show absorption features due to water vapor. In addition some absorption due to carbon dioxide at 2μ is expected and there are strong CO_2 absorption features near 2.7μ. Because gaseous absorption takes place not only above the clouds but through multiple reflection within the clouds, we did not exactly correct for this effect. One cannot practically correct for the multiple scattering within the clouds by assigning an effective single scattering albedo to the gaseous absorption component, because the spectral resolution was much larger than the spectral domain over which the gaseous absorption is constant. We performed our water vapor absorption corrections by comparing the value of R_λ at two spectral positions, one position expected to have

very little gaseous absorption and the other a large amount. Furthermore the clouds were expected to have approximately the same intrinsic value for R_λ at the two wavelength positions. In the 1.2 - 2.5μ region we compared R_λ values at 1.28μ with either 1.35μ or 1.38μ, while for the 2.4 - 3.6μ domain we considered values either at 2.50 or 2.55 with ones at either 2.60 or 2.61μ. The ratio of the values of R_λ were equated to ratios of gaseous transmissivities calculated by Wyatt, Stull and Plass (1962). The comparison was made at pressures and temperatures closest to the cloud top conditions, as inferred from the cloudtop altitude, and in all cases at an effective resolution of $100cm^{-1}$. While this resolution is somewhat poorer than the resolution of the spectrometer it was found to yield the most consistent results. In part the need to employ $100cm^{-1}$ resolution is a reflection of the breakdown of the theoretical statistical model at finer resolutions, as indicated by the appearance of high frequency features whose amplitude is too large. From the comparison with Wyatt et al.'s tables we derived an effective water vapor abundance, W, and used this amount to estimate the effective gaseous transmission at other wavelengths. At wavelengths where there is more absorption by the cloud aerosols, there is less multiple scattering and in this sense the transmission correction is an overestimate. This circumstance pertains at most of the other wavelengths

and the true cloud reflectivity in general should lie between the uncorrected and "corrected" values.

Absorption effects by carbon dioxide were much more localized in the spectrum. For the strong absorption band near 2.7μ, we derived an effective amount of CO_2 and an average pressure by allowing for the path down to and up from the cloud top and estimating the effective path in the clouds from the water vapor absorption amount. The latter can be related to the atmospheric temperature where the absorption takes place, as discussed below, and to the pathlength with the help of the U.S. Standard Atmosphere Supplements (1966). For the much smaller corrections within the 2μ band, we used the water vapor absorption amounts as a guide in a less rigorous fashion. Transmission corrections were then obtained from the tables of Stull, Wyatt and Plass (1963).

Fortunately the angular measurements refer to the pathlengths of nearly constant angle of incidence and reflection and so to first order they require no absorption correction. However because some absorption takes place through multiple scattering the effective atmosphere transmission may have an azimuthal dependence. This effect is very difficult to correct for and no attempt was made to do so.

5. Discussion of gaseous absorption corrections

In Table 1 we summarize the water vapor amounts, W_{eff}, deduced from Blau et al.'s spectra. The first column gives the figure number of the spectra in their final report. P is the pressure assumed in deriving W_{eff}. Also given are the cloud type and the cloudtop altitude. Using the U.S. Standard Atmosphere Supplements (1966), we have estimated the temperature at the cloudtop, T_{cd}, from its altitude.

To assess the contribution of multiple scattering within the clouds to the observed water vapor absorption features, we have computed the equivalent amount of water vapor W_{ref} which the sunlight passes through above the clouds, on its path down to the cloudtop and up to the airplane. In performing the calculation we have assumed the atmosphere to be saturated. In addition we have corrected for the difference in the value between the pressure used in obtaining W_{eff} and the actual cloud top pressure by assuming that pressure and gas amount are equally effective in causing absorption. For the first three spectra of the 1.2 - 2.5μ region W_{ref} is significantly smaller than W_{eff}. Hence most of the absorption takes place in the clouds. A confirmation of this deduction is obtained by comparing the values of W_{eff} for the two sets of spectra from Fig. 55. The value of W_{eff} obtained for the larger angle of incidence is smaller than that for the

TABLE 1

WATER VAPOR AMOUNTS AND CLOUD TEMPERATURES

Fig.	θ_o (Degrees)	θ (Degrees)	Cloud	Cloudtop Altitude (kft)	P (atm)	W_{eff} (pr cm)	W_{ref} (pr cm)	T_{scat} (°K)	T_{cd} (°K)
				$\lambda = 1.2 - 2.5\mu$					
55	64	0	cirrus	38	0.5	0.26	0.0023	247	216
55	71	0	cirrus	38	0.5	0.20	0.0031	245	216
53	44	0	cumulus	28	1.0	0.68	0.014	260	233
51	52	0	thick cirrus over cumulus	25	0.5	0.10	0.061	239	238
				$\lambda = 2.4 - 3.6\mu$					
18	48	0	cumulus	50	0.2	0.0036	.016		220
20	52	80	cirroform*	50	0.2	0.019	.025		216

*Part of Hurricane Gladys.

smaller angle of incidence; this finding is opposite to the expectation for absorption taking place above the cloud, but in accord with predictions for multiple scattering within a cloud layer (Chamberlain, 1965). Such a phenomenon is also present for at least some of the gaseous absorption features of Venus (Chamberlain and Kuiper, 1956).

On the other hand, W_{ref} is larger or comparable to W_{eff} for the two spectra pertaining to the 2.4 - 3.6μ region. This results in part from the cloudtops being located high within the stratosphere where the water vapor abundance is only a few percent of the saturation abundance. For these spectra we can conclude that the fraction of the cloud significantly contributing to the scattering lies within the stratosphere and therefore we are surely viewing ice particles. The relatively small depth of penetration for these spectra is a result of the highly absorbing nature of ice aerosols at 2.5 and 2.6μ, the wavelengths at which W_{eff} was obtained.

To derive an estimate of the depth of penetration for the other clouds, we have computed T_{scat}, the base temperature required within a saturated atmosphere so that light traveling on a straight line down to and up from this level at a 60° angle would experience the observed amount of absorption. Since the actual pathlength within the clouds is more tortuous, T_{scat} is probably a slight overestimate of the

level of line formation. We see that for the first three spectra T_{scat} is substantially larger than T_{cd}, implying substantial penetration within the clouds. At the wavelengths used to derive W_{eff} for these spectra the cloud aerosols are essentially transparent.

6. Analysis of the cloud spectra

Our theoretical spectra are functions of three parameters: the characteristic particle size r_m, the optical thickness τ of the clouds, and the phase of the cloud, i.e., whether the aerosols are liquid water or ice. Below we attempt to estimate each of these parameters by comparing the theoretical and observed spectra.

In Figs. 8 and 9 Blau et al's observations of a cirrus cloud in the 1.2 to 2.5μ wavelength region are compared with theoretical spectra for an ice cloud. The observations correspond to Blau et al.'s Fig. 55 for an angle of incidence of 71°. Circles and solid bars represent the average values and standard deviations of the reflectivity R (eq. 3) after correction for gas absorption, while the uncorrected observations are indicated by triangles and dotted bars in the cases where they differ significantly from the corrected values. As explained above, the absorption corrections may be overestimates in regions where the cloud aerosols strongly absorb. In this case the true reflectivity will be somewhere between

the corrected and uncorrected values. The theoretical curves in each portion of the diagrams correspond to various choices for the optical depth; the particle size parameter is varied by a factor of 2 between successive sections. Comparing the four sections of Figs. 8 and 9, we see that the observations permit the determination of a well defined value for r_m, 16μ.

In all of the figures the optical depth refers to $\lambda = 1.2\mu$; however, the wavelength dependence of τ is small since we always consider a distribution of particle sizes with $x_m > 1$. In determining τ, values of R between 1.2 and 1.4μ are of particular use: the theoretical curves differ at these wavelengths by a maximum amount. For the cloud observations illustrated in Fig. 9 a value $\tau \sim 10$ appears to give the best fit. However, the optical depth is more difficult to estimate than the particle size, and this derived optical depth should probably only be regarded as a lower limit. Danielson, Moore and van de Hulst (1969) have argued, from observations and computations, that condensation nuclei limit the cloud reflectivity at wavelengths where ice and water do not effectively absorb $[1 - \omega \lesssim 10^{-3}]$.

As mentioned above the absorption features of water and ice are displaced somewhat from one another. For example peak absorptions and hence minimum values of R occur at 1.45 and 1.95μ for water and at 1.52 and 2.00μ for ice. As a result the theoretical water spectra do not fit the observed

spectra in these regions. On the other hand, there is some indication that a local maximum in R occurs at 2.2μ, a position expected for water clouds, rather than 2.3μ, the place for ice clouds. A similar situation was found in some of the other spectra. This could be understood in terms of a mixed phase model with ice predominating near the top of the cloud, but the quality of the present data did not warrant calculations for such a model.

In a similar fashion we analyzed several other observed spectra. The results are summarized in Table 2. It is encouraging to see that the same cloud properties were found from observations of the same cloud viewed at two different solar illumination angles (Fig. 55). An interesting feature of Table 2 is the similar value for r_m found for the various ice cloud spectra. The deduced average particle radius of 16μ, or diameter of 32μ, is consistent with values typically obtained from direct sampling measurements of ice clouds.

TABLE 2

DEDUCED PROPERTIES OF SOME OBSERVED TERRESTRIAL CLOUDS

Blau's Fig.	θ_o	Cloud	Deduced Properties Phase	$r_m(\mu)$	τ
		λ = 1.2 to 2.5μ			
55	71	cirrus	ice>	16	10
55	64	cirrus	ice	16	10
53	44	cumulus	water	8	4
51	52	thick cirrus over cumulus	ice	16	10
		λ = 2.4 to 3.6μ			
18	48	cumulus	ice	16	>5
20	52	cirroform	ice	16	>5

In Fig. 10 we consider the degree to which multiple scattering occurs in the 2.5 to 3.5μ spectral region, where the cloud aerosols are highly absorbing. The curves illustrated are for an optical depth of unity and a large enough optical depth ($\tau = 128$) to be considered equivalent to an infinite value; we obtained almost identical results for all optical depths in excess of 10. The dashed curve represents photons scattered only once, the dotted curve photons scattered n times ($n \geq 1$) with the first n-1 scattering events occuring within the diffraction peak (Hansen, 1969b), while the solid curve represents all the photons reflected from the cloud. We see that even if the dotted curve is considered

as representing single scattering, single scattering computations are inadequate to describe the reflectivity in this highly opaque part of the spectrum.

In Fig. 11 we compare computed cloud spectra for $\tau \geq 10$ with data given in Blau et al.'s Figs. 18 and 20. The theoretical curves correspond to various choices of r_m. The data points between 2.5 and 2.6μ indicate a particle size of about 16μ in both cases. Near 3μ the observations and calculations are not in good agreement; this disagreement is discussed in detail in § 8.

Finally we note that sample calculations of blackbody thermal emission from the clouds showed this contribution to be very small compared to reflected sunlight, even at the longest wavelengths of observation.

7. Analysis of the clouds' angular scattering

In this section we attempt to assess the information content of the clouds' angular scattering properties. As mentioned earlier, observations were made at nearly constant angles of incidence and reflection but with varying azimuth and hence scattering angles. In Figs. 12 and 13 we contrast the theoretical single scattering behavior of water clouds with the complete multiple scattering behavior. The computations were made for angles of incidence and reflection of 60° and 80°, respectively. In Fig. 12 the reflectivity has been calculated for a distribution of water particles having a mean size r_m of 2μ, while Fig. 13 pertains to a value of 16μ for r_m. For the larger size particles, we defined single scattering to include photons scattered (n-1) times

in the diffraction peak ($n \geq 1$) before suffering a final scattering back out of the cloud. Since the 2μ size particles do not have a striking diffraction peak, we defined single scattering for them in the conventional manner.

We see that the effect of multiple scattering is to wash out features such as the rainbow and to greatly diminish the angular variation of R. Even for an optical depth of unity the actual scattering behavior is markedly different from that of single scattering. At an optical depth of 16 the scattering behavior is quite close to that for an infinite optical depth. On the basis of their high albedo in the visible we know most clouds have an optical depth of 16 or more. In this event a knowledge of the exact value of the optical depth is not too important for being able to predict the reflectivity properties.

In Fig. 14 we compare theoretical calculations with the angular dependence exhibited by a cumulus cloud whose top was at 4 kft. This cloud was part of Hurricane Gladys. For each data point the angle of reflection was 80° but the angle of incidence varied between 56° and 64°. The theoretical computations were performed for spherical water particles at the angles appropriate for each observation, and the theoretical points were joined together by straight lines. As mentioned above, no correction for gas absorption was made.

All the theoretical spectra are normalized to fit the data point at the lowest value of $(\phi - \phi_o)$. A particle size of 8μ appears to yield the best fit to the measurements, a result compatible with typical direct sampling measurements of cumulus clouds. Unfortunately, the absorption corrections were so large we were unable to meaningfully analyze the spectra to confirm this deduction.

Angular computations in the 2.4 to 3.6μ region are shown in Figs. 15 and 16. The calculations were made for spherical ice particles with the realization that this may lead to a very poor approximation to the true angular scattering behavior of ice clouds. In Fig. 15 a mean particle radius r_m of 16μ wasused and the optical depth varied. In Fig. 16 the particle size is varied, while the optical depth was set equal to 32. In all cases the angles of incidence and reflection are 50° and 80° respectively. We see that for cases of intermediate aerosol absorption, e.g., $r_m = 16\mu$ and $\lambda = 2.72\mu$, the exact solutions most clearly preserve such features as the rainbow peak and exhibit the strongest dependence upon particle size. When the aerosol absorption is relatively small, many scattering events occur leading to a smooth, featureless angular behavior. When the aerosol absorption is very large the rainbow is not present even for single scattering.

In Fig. 17 we compare theoretical and observed cloud reflectivities for an angle of reflection of 80° and an

angle of incidence between 44° and 56°. The observations pertain to cirroform clouds whose tops were at 43 kft. They were part of Hurricane Gladys. The theoretical curves have the same meaning as those in Fig.14, except that Fig. 17 is for spherical ice particles. A particle radius of 16μ, a value found typical for cirrus clouds from the spectral analysis, gives no worse a fit to the data than other sizes. The calculations at all 3 wavelengths were made with the optical constants given by Irvine and Pollack; however, if we accept the modification in the optical constants which is indicated by the results in § 8, then the theoretical calculations at $\lambda = 3.10\mu$ would be changed and brought into better agreement with the observations. At 3.10μ the primary effect of the new optical constants is to increase the Fresnel reflection in the backward direction; this would increase the theoretical reflectivity at the two right-most data points in Fig. 17.

8. Optical constants of ice near $\lambda = 3\mu$

In this section we reconsider the ice cloud spectra near $\lambda = 3\mu$ where the calculations and observations are not in good agreement, and we suggest one possible explanation for the discrepancy.

A minimum in the observed spectra (Fig. 11) occurs at about 2.9μ in wavelength and a maximum around 3.1μ. These features are particularly prominent in the right hand graph. This may at first appear surprising since ice has its maximum absorption at 3.1μ (Irvine and Pollack, 1968). Blau and Espinola (1969) first pointed out the minima in the spectra and correctly attributed it to the anomalous dispersion of n_r, which is discussed above. A local maxima in the reflectivity is expected near 3.1μ for similar reasons. Our computed spectra qualitatively show these effects, but particularly for the right hand graph (Fig. 11) they fail to quantitatively match the observations. Blau and Espinola encountered a similar

difficulty in explaining the minimum and suggested that Irvine and Pollack's value of n_r be revised near this wavelength position.

We have also considered the possibility of revising Irvine and Pollack's optical constants for ice in the vicinity of the strong 3.1μ feature. We have attempted to do this in a consistent fashion by relating changes in the real part of the index of refraction, n_r, to changes in the imaginary part n_i. Spitzer and Kleinman (1961) have given relationships between n_r and n_i under the assumption that individual absorption bands may be considered as classical oscillators and have obtained a very good fit to reflection measurements of strong infrared bands of quartz. Assuming that the 3.1μ band is a dominant feature at nearby wavelengths and neglecting small differences between the value of the frequency at the desired positions and the central frequency of the band, we have simplified Spitzer and Kleinman's formulas to the following general form:

$$n_r \, n_i = \frac{p\Gamma^2}{(\Delta\lambda)^2+\Gamma^2} \tag{4}$$

$$n_r^2 - n_i^2 = A + \frac{2p\Gamma \, \Delta\lambda}{(\Delta\lambda)^2+\Gamma^2} \tag{5}$$

where p is the maximum value of the product of $n_r n_i$, Γ one half the value of the width between half maximum points of $n_r n_i$, Δλ the difference in wavelength between the value of interest and the position of the maximum, and A is a constant. These formulae give a good fit to the water and ice data of Irvine and Pollack near the 3μ absorption feature.

For the ice constants given by these authors p is about 0.42, and Γ about 0.15μ. The constant A is readily found by applying the second formula to wavelengths significantly shortward of 3μ; we find A is 1.66.

In modifying the indices of refraction given by Irvine and Pollack we assumed that Γ was unchanged and varied the only remaining free parameter p by various scale factors c. We have modified the published data between 2.8μ and 3.6μ because this is the region dominated by the 3.1μ band. In addition the published indices shortward of 2.8μ were based on a different set of measurements than those used at 2.8μ and longward. These first set were checked against other measurements and found to be in good agreement. The results of two trial modifications are given in Fig. 18 along with the original values. In addition the effects of the modified indices on the single scattering albedo $\tilde{\omega}$ and the angular asymmetry parameter $\langle \cos \theta \rangle$ are shown. At short wavelengths the value c = 2 led to values of n_r less than 1 and so this portion of the curve has not been drawn.

Since the optical parameters have not been changed shortward of 2.8μ, the deduced characteristic particle sizes and the lower limit on the optical depth will still hold. We were able to deduce these from the data points between 2.47μ and 2.65μ. Fig. 19 shows theoretical spectra for Blau's Figs. 18 and 20 based on values of c = 1 (the old optical constants), 1.6, and 2. We see that a value of c of about

1.6 leads to a good fit of the spectra for both Figs. 18 and 20.

Some justification for our method of varying the ice constants is provided by the following: For wavelengths $< 2.8\mu$ the optical constants of Irvine and Pollack were based on several sources of data which agreed with one another. However, for $\lambda \geq 2.8\mu$ Irvine and Pollack had only one source for the ice absorption coefficients and this source gave water absorption coefficients for $\lambda \sim 3\mu$ which were $\sim$ 60% less than the values obtained by several other experimenters. Thus the proposed revision of the indices of refraction seems quite reasonable.

9. Summary

This study indicates that characteristic broad band absorption features in light scattered by clouds can be used to help identify the scattering material and to determine the particle size and cloud optical depth. The results are consistent with the assumption that it is adequate to employ the spherical particle approximation in calculating the spectral reflectivity. As far as the angular behavior is concerned, not enough accurate observations are available for an adequate analysis of the theory. More extensive measurements on atmospheric clouds are desirable, as well as carefully controlled laboratory observations along the lines of the recent measurements by Zander (1968) and Plummer (1969).

Acknowledgements

We are very indebted to Henry Blau and Ronald Espinola for several useful discussions and for sending us some of their original data. This research was supported in part at Cornell University by NASA grant NGR 33-010-082 and NSF grant GA-1086. During the course of this work J. Hansen was supported consecutively by a NAS-NRC Research Associateship supported by NASA at the Institute for Space Studies, a National Science Foundation Fellowship at the Sterrewacht, Leiden, Netherlands, and by NASA grant NGR- 33-008-012 through Columbia University.

APPENDIX

The following shortcuts in the numerical work have been tested and found useful for the multiple scattering computations:

(a) For large particles ($x = 2\pi a/\lambda \geq 25$) there is a sharp diffraction peak in the phase function which necessitates a large number of terms in the cosine expansion of the scattering function and a large number of points in the integrations over $\mu = \cos\theta$. However, in the case of conservative scattering we have shown elsewhere (Hansen, 1969b; see also Potter, 1969) that the photons scattered into the forward spike may be approximated as being unscattered by truncating the forward peak from the phase function and reducing the interaction optical thickness τ such that

$$\tau' = (1 - F)\,\tau \tag{A1}$$

where τ' is the optical thickness to be used with the truncated phase function, F is the fraction of photons scattered into the forward peak,

$$F = \int_{4\pi} (p - p')\,\frac{d\omega}{4\pi}, \tag{A2}$$

and p and p' are the untruncated and truncated phase functions, respectively. For conservative scattering this approximation

introduces large errors in the reflected intensities only for small total scattering angles ($\Theta \sim 0^{\circ}$); it introduces errors of a few percent if the total scattering angle corresponds to a sharp feature in the phase function (such as the glory) and it also introduces errors of a few per cent if the incident or emergent angle is near grazing (Θ, Θ_o, $\sim 90^{\circ}$) elsewhere the error is $\leqslant 1\%$.

In the case of nonconservative scattering the single scattering albedo, ω, must be scaled such that

$$\omega' = \frac{1}{1 + \frac{1 - \omega}{\omega(1 - F)}} \qquad \text{(A3)}$$

because the assumption that photons in the forward peak should be treated as unscattered implies that the absorption cross section is unchanged and the scattering cross section reduced by the factor 1 - F. Several tests of this approximation were made and it was found to become increasingly accurate as ω decreased. Even in the wavelength region $\sim 3\mu$ where often $\sim 80\%$ of the single scattered photons were cut off with the truncating of the diffraction peak, the error introduced was $\leqslant 1\%$ except for scattering angles $\sim 0^{\circ}$.

(b) In the expansion of the scattering function in cosines, we write:

$$S(\tau;\ \mu,\ \phi;\ \mu_o,\ \phi_o) = \sum_{m=0}^{\infty} S^m(\tau;\ \mu,\ \mu_o) \cos m\ (\phi - \phi_o) \qquad \text{(A4)}$$

where μ_o and μ denote the cosine of the angles of incidence and reflection, respectively and ϕ_o and ϕ are the corresponding azimuth angles. The number of terms, M, needed to obtain an accuracy within 1% for all μ and μ_o with a strongly anisotropic phase function is typically about one hundred. However, the range of μ and μ_o for which the numerical value of $S^m(\mu, \mu_o)$ is not negligible decreases as m increases until for $m \sim M$ only $S(\tau; \mu \sim 0\ \mu_o \sim 0)$ is significant. If $S(\tau; \mu, \phi, \mu_o, \phi_o)$ is to be calculated at N values of μ on the interval (0,1) and N values of μ_o then $S^o(\tau; \mu, \mu_o)$ must be computed at N^2 points and in the integrations over μ which include $S^o(\tau; \mu, \mu_o)$ as a factor, N points are employed; however the number of points required decreases steadily as m increases until for $S^M(\tau; \mu, \mu_o)$ calculations are only needed for one point and only one point is needed in the integrations. For a given accuracy specification it is easy by numerical testing to find the number of points at which $S^m(\tau; \mu, \mu_o)$ must be calculated and included in the integrations. A factor of 2 - 3 in computer time may be saved with an introduction of errors ~ 1 - 2%.

(c) The strongest azimuthal dependence arises from single scattered photons but an analytic expression exists for the intensity due to these photons (Hansen, 1969a) and hence considerable computing time may be saved by writing

$$S(\tau;\mu,\phi;\mu_o,\phi_o) = S_{ss}(\tau;\mu,\phi;\mu_o,\phi_o) + \sum_{m=0}^{\infty} [S^m(\tau,\mu,\mu_o) - S^m_{ss}(\tau;\mu,\phi_o)] \cos m(\phi - \phi_o) \quad \text{(A5)}$$

where the subscript ss labels the contributions of single scattering to the S function. Typically the number of terms needed in (A5) is ~ 50% of the number required with (A4) to achieve the same accuracy.

(d) Several additional ways to save computer time, which we found by numerical experimentation, can be shown to have a firm theoretical basis from work of van de Hulst (forthcoming book). van de Hulst shows that each term in the cos m $(\phi - \phi_o)$ expansion may be thought of as having an effective albedo for single scattering and this albedo decreases steadily as m increases. Some consequences are: the doubling process for terms with $m \geq 1$ may be initiated at an optical thickness $\tau_o \sim 2^{-15}$ rather than 2^{-25}, for $m \geq 1$ the asymptotic value of the scattering function is obtained already at $\tau \sim 8$; for $m \geq M/4$ the sum of the infinite series occurring in the doubling equations may be replaced by the value of the first term. These simplifications may easily reduce the computing time by a factor ~ 3.

If all four of the above methods for reducing the computer time are employed the total time saving is not the product of the factors which each gives alone because there is considerable overlap. In the computations for this paper (performed on an IBM 360/95) we always employed (d) and for the particle size distributions with $r_m = 16\mu$ and 32μ we

used (a). All of the above methods may be worthwhile for slower computers and especially for problems such as line formation and the multiple scattering of polarized light.

Note added in revision: Dave (1970) has independently shown that the number of terms required in the Fourier expansion depends strongly on μ and μ_0 [shortcut (b) above] and he has presented graphical illustrations of this. Dave also makes use of the fact that the effective albedo decreases toward higher terms in the Fourier expansion [shortcut (d)].

FIGURES

Fig. 1 Single scattering phase functions for a size distribution of transparent spherical particles with a real refractive index typical of water and ice in the near infrared; the curves show the effect of changing the characteristic particle size. In Figs. 1-3 the vertical scales apply to the uppermost curve on the left side and the scales for the other curves may be obtained by multiplication by a power of 10 such that the horizontal bar on each curve occurs at $p(\theta) = 1$.

Fig. 2 Single scattering phase functions for a size distribution of spherical particles showing the effect of absorption within the particles for large particles ($x_m = 32$) and particles of moderate size ($x_m = 2$)

Fig. 3 Single scattering phase functions for a size distribution of spherical particles showing the effect of changing the real part of the refractive index for large particles with no absorption (left), for particles of moderate size with no absorption (upper right), and for large particles with moderate absorption (lower right).

Fig. 4 Single scattering albedo for a cloud of spherical water particles for five different particle size distributions.

Fig. 5 Same as Fig. 4 for spherical ice particles.

Fig. 6 Asymmetry factor of the phase function for a cloud of spherical water particles for five different particle size distributions.

Fig. 7 Same as Fig. 6 for spherical ice particles.

Fig. 8 Theoretical cloud reflectivities for $\theta = 0$, $\theta_o = 71^o$ and $\phi - \phi_o = 180^o$ for five cloud optical thicknesses and two size distributions of spherical ice particles. The circles and solid bars represent observations by Blau, et al. of cirrus clouds at 38,000 feet after correction for gas absorption; the uncorrected observations are indicated by triangles and dotted bars in the cases where they differ significantly from the "corrected" values.

Fig. 9 Same as Fig. 8 for two additional particle size distributions.

Fig. 10 Theoretical cloud reflectivities for $\theta = 0^o$, $\theta_o = 48^o$ and $\phi - \phi_o = 180^o$, for two cloud optical thicknesses for the size distribution of spherical ice particles having the characteristic particle size $r_m = 16\mu$.

Fig. 11 Theoretical cloud reflectivities for $\tau \geq 10$ for five size distributions of spherical ice particles. The circles represent observations by Blau, et al. of "cumulus" clouds at 50,000 feet after correction for gas absorption; the uncorrected observations are indicated by triangles.

Fig. 12 Theoretical cloud reflectivities as a function of azimuth angle for $\theta = 80^{\circ}$ and $\theta_o = 60^{\circ}$ for a size distribution of spherical water particles with $r_m = 2$.

Fig. 13 Same as Fig. 12 for a size distribution with $r_m = 16$.

Fig. 14 Theoretical and observed cloud reflectivities for $\theta = 80^{\circ}$ and $56 \leq \theta_o \leq 64$ normalized to unity at the smallest observed value of $\phi - \phi_o$. The theoretical calculations are for water particles at values of θ, θ_o, and $\phi - \phi_o$, correct for each observed point and connected by straight lines. The computations were made for $\tau = 32$, but are approximately valid for $\tau \geq 10$. The observations by Blau, et al. were made on cumulus clouds at 4,000 feet above Hurricane Gladys.

Fig. 15 Theoretical cloud reflectivities as a function of azimuth angle for $\theta = 80^{\circ}$ and $\theta_o = 50^{\circ}$ for a size distribution of spherical ice particles having $r_m = 16\mu$.

Fig. 16 Same as Fig. 15 but for four particle size distributions and for only one cloud optical thickness ($\tau = 32$).

Fig. 17 Theoretical and observed cloud reflectivities for $\theta = 80^{\circ}$ and $44^{\circ} \leq \theta_{o'} \leq 56^{\circ}$ normalized to unity at the smallest observed value of $\phi - \phi_o$.

Fig. 18 The optical constants for ice are shown in the upper part of the figure with the solid curve representing the data of Irvine and Pollack (1968); the other two curves were obtained by multiplying Irvines and Pollack's $n_r n_i$ by the factor c in the interval $2.8 \leq \lambda \leq 3.6$. The lower part of the figure shows the single scattering parameters $< \cos \theta >$ and ω for the three sets of optical constants.

Fig. 19 Same as Fig. 11 with the theoretical curves for the size distribution having $r_m = 16\mu$; the three curves correspond to the three choices of c shown in Fig. 18.

REFERENCES

Blau, H. H., and R. P. Espinola, 1965: Infrared spectral properties of high-altitude clouds. Arthur D. Little, Inc., Rept., Cambridge, Massachusetts, 117 pp.

_____ and _____, 1969: Spectral property of clouds from 2.5 to 3.5 microns. Preprint.

_____, _____, and E. C. Reifenstein, 1966: Near infrared scattering by sunlit terrestrial clouds. Appl. Opt., 5, 555-564.

Chamberlain, J. W., 1965: The atmosphere of Venus near her cloud tops. Astrophys. J., 141, 1184-1205.

_____, and G. P. Kuiper, 1956: Rotational temperature and phase variation of the carbon dioxide bands of Venus. Astrophys. J., 124, 399-405.

Danielson, R E., D. R. Moore, and H. C. van de Hulst, 1969: The transfer of visible radiation through clouds, J. Atmos. Sci., 26, 1078-1087.

Dave, J. V., 1969a: Effect of coarseness of the integration increment on the calculation of the radiation scattered by polydispersed aerosols. Appl. Opt., 8, 1161-1167.

_____, 1969b: Effect of varying integration increment on the computed polarization characteristics of the radiation scattered by polydispersed aerosols. Appl. Opt., 8, 2153-2154.

_____, 1969c: Scattering of visible light by large water spheres. Appl. Opt. 8, 155-164.

_____, and J. Gazdag, 1970: A modified Fourier transform method for multiple scattering calculations in a plane-parallel Mie atmosphere. Submitted to Appl. Opt.

Deirmendjian, D., 1964: Scattering and polarization properties of water clouds and hazes in the visible and infrared. Appl. Opt. 3, 187-196.

_____, 1969: Electromagnetic Scattering on Spherical Polydispersions. New York, Elsevier, 290 pp.

_____, and R. J. Clasen, 1962: Light scattering on partially absorbing homogeneous spheres of finite size. R-393-PR, The Rand Corporation, Santa Monica, Calif., 44 pp.

Hansen, J. E., 1969a: Radiative transfer by doubling very thin layers. Astrophys. J., 155, 565-573.

_____, 1969b: Exact and approximate solutions for multiple scattering by cloudy and hazy planetary atmospheres. J. Atmos. Sci., 26, 478-487.

_____, and H. Cheyney, 1968: Near infrared reflectivity of Venus and ice clouds. J. Atmos. Sci., 25, 629-633.

_____, and _____, 1969: Theoretical spectral scattering of ice clouds in the near infrared. J. Geophys. Res., 74, 3337-3346.

Irvine, W. M., and J. B. Pollack, 1968: Infrared optical properties of water and ice spheres. Icarus, 8, 324-360.

Kattawar, G. W., and G. N. Plass, 1967: Electromagnetic scattering from absorbing spheres, Appl. Opt., 6, 1377-1382.

Plummer, W. T., 1969: Near-infrared reflection spectra of artificial cumulus clouds. Appl. Opt., 8, 2079-2081.

Pollack, J. B., and C. Sagan, 1968: The case for ice clouds on Venus. J. Geophys. Res., 73, 5943-5949.

Potter, J. F., 1969: The delta function approximation in radiative transfer theory (to be published).

Sagan, C., and J. B. Pollack, 1967: Anisotropic nonconservative scattering and the clouds of Venus. J. Geophys. Res., 72, 469-477.

Spitzer, W. G. and D. A. Kleinman, 1961: Infrared lattice bands of quartz. Phys. Rev., 121, 1324-1335.

Stull, V. R., P. J. Wyatt, and G. N. Plass, 1963: The infrared absorption of carbon dioxide. Aeroneutronic rept. no. SSD-TDR-62-127, III.

U.S. Standard Atmosphere Supplements, 1966: prepared by ESSA, NASA, and U.S. Air Force.

van de Hulst, H. C., 1957: Light Scattering by Small Particles. New York, John Wiley, 470 pp.

_____, 1963: A new look at multiple scattering. Institute for Space Studies, NASA, New York, Rept. 81 pp.

Wyatt, P. J., V. R. Stull, and G. N. Plass, 1962: Infrared absorption of water vapor. Aernutronic Rept. no. SSD-TDR-62-127, II.

Zander, R., 1968: Additional details on the near-infrared reflectivity of laboratory ice clouds. J. Geophys. Res., 73, 6581-6584.

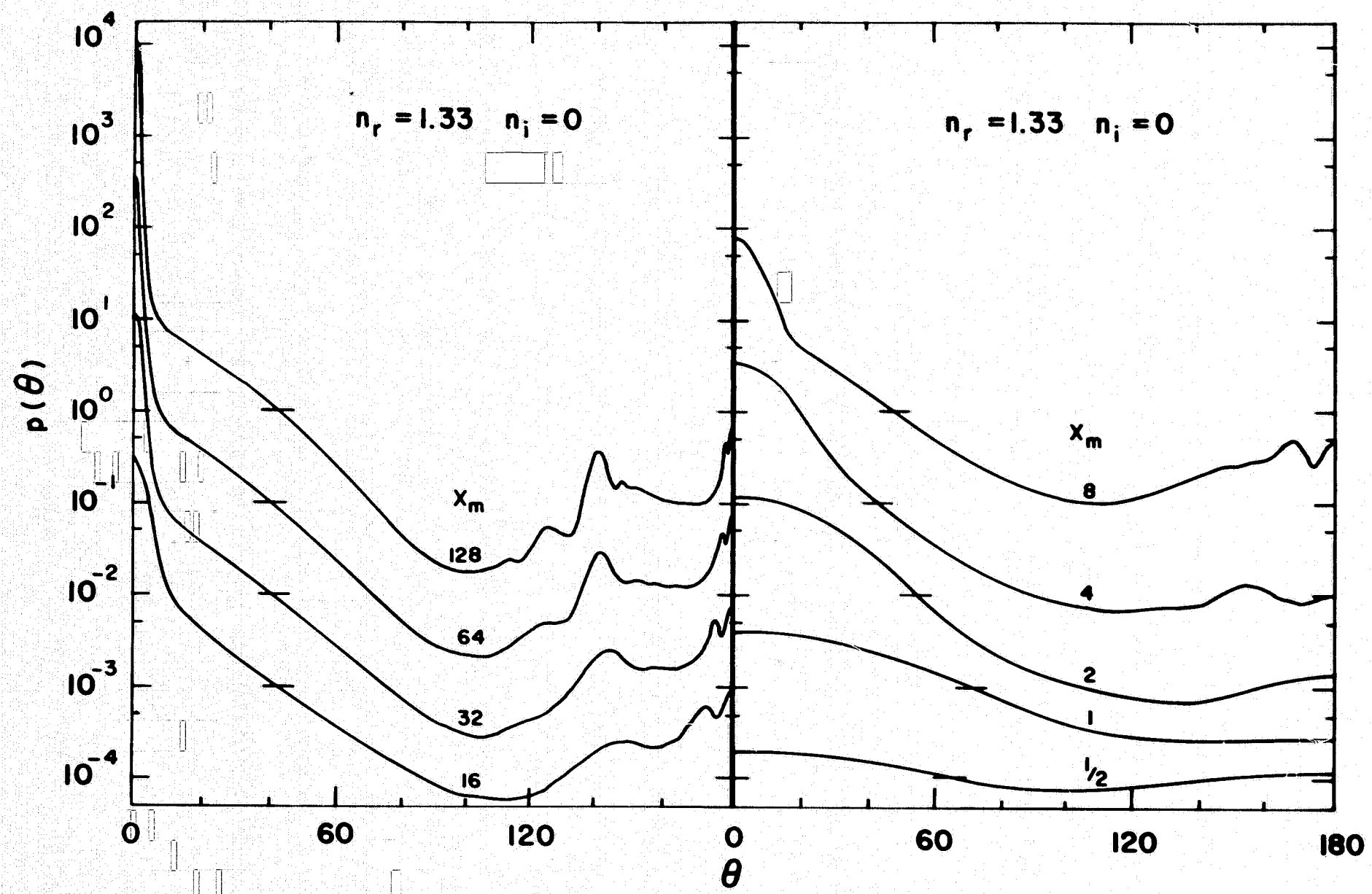
$n_r = 1.33$ $n_i = 0$
$n_r = 1.33$ $n_i = 0$
$p(\theta)$
10^4
10^3
10^2
10^1
10^0
10^{-1}
10^{-2}
10^{-3}
10^{-4}
x_m
128
64
32
16
x_m
8
4
2
1
1/2
0
60
120
0
60
120
180
θ

Fig. 1

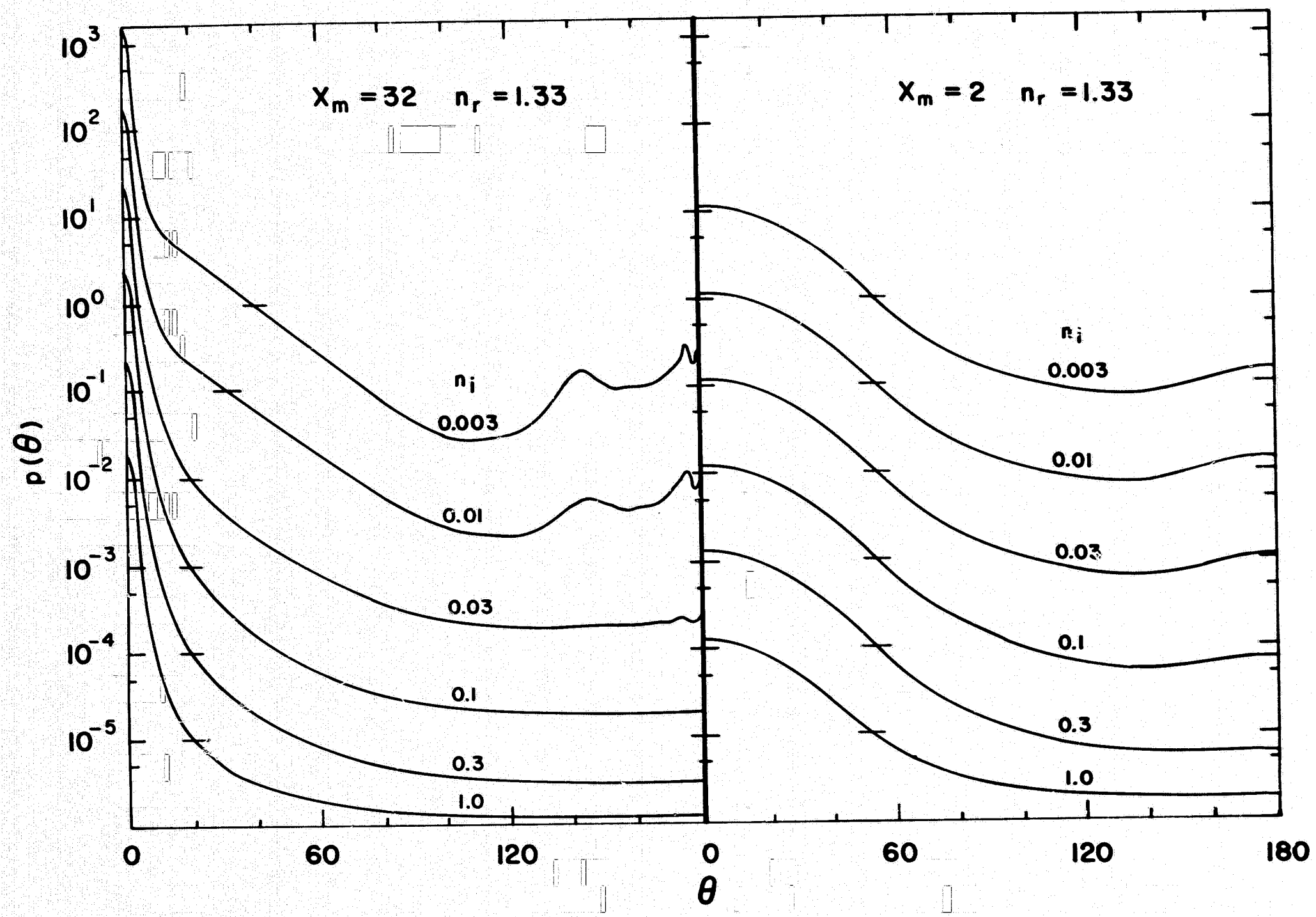
$X_m = 32$ $n_r = 1.33$
$X_m = 2$ $n_r = 1.33$
n_i
0.003
0.01
0.03
0.1
0.3
1.0
$p(\theta)$
10^3
10^2
10^1
10^0
10^{-1}
10^{-2}
10^{-3}
10^{-4}
10^{-5}
0
60
120
180
θ

Fig. 2

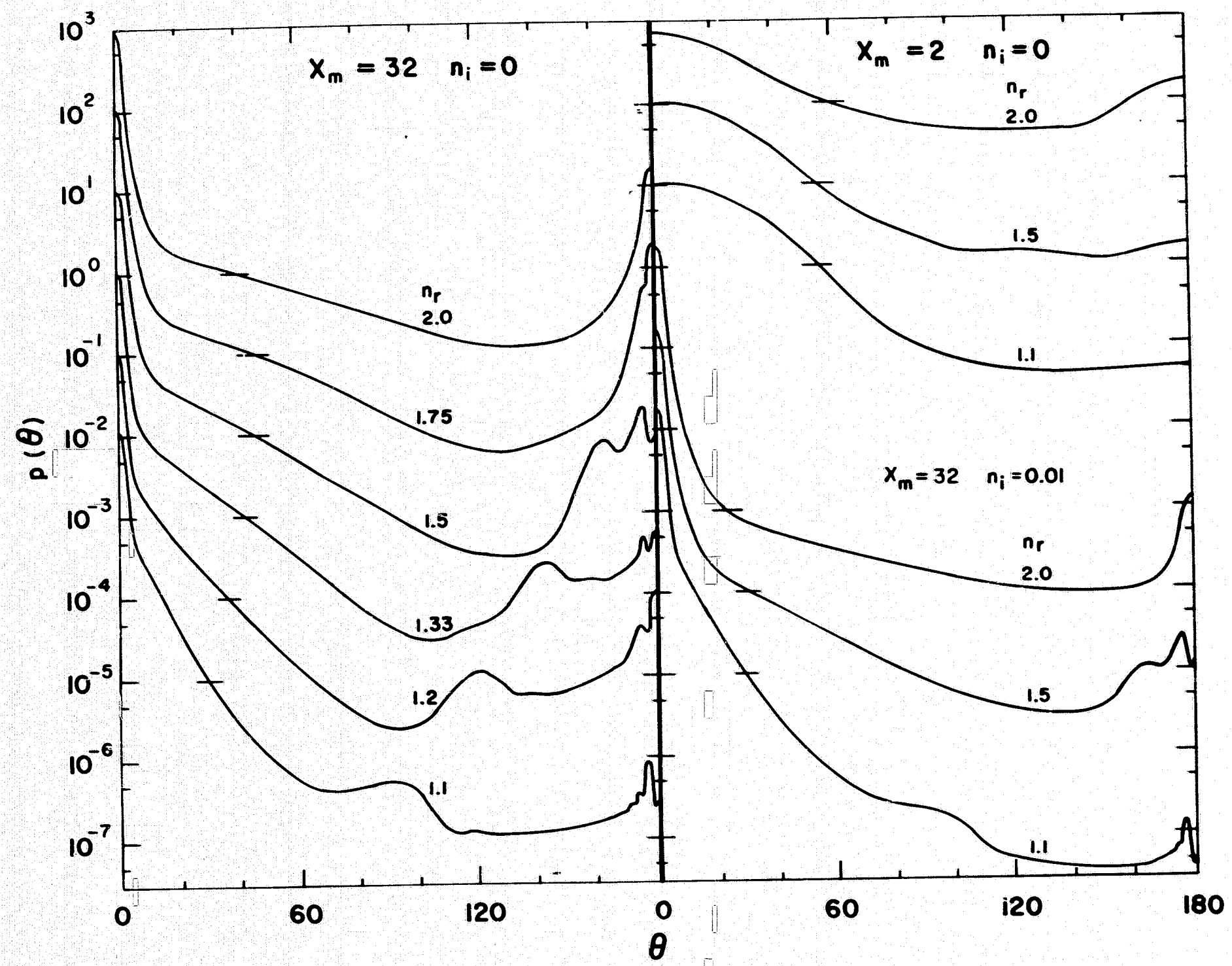
$X_m = 32$ $n_i = 0$
n_r
2.0
1.75
1.5
1.33
1.2
1.1
$X_m = 2$ $n_i = 0$
n_r
2.0
1.5
1.1
$X_m = 32$ $n_i = 0.01$
n_r
2.0
1.5
1.1
$p(\theta)$
10^3
10^2
10^1
10^0
10^{-1}
10^{-2}
10^{-3}
10^{-4}
10^{-5}
10^{-6}
10^{-7}
0
60
120
0
60
120
180
θ

Fig. 3

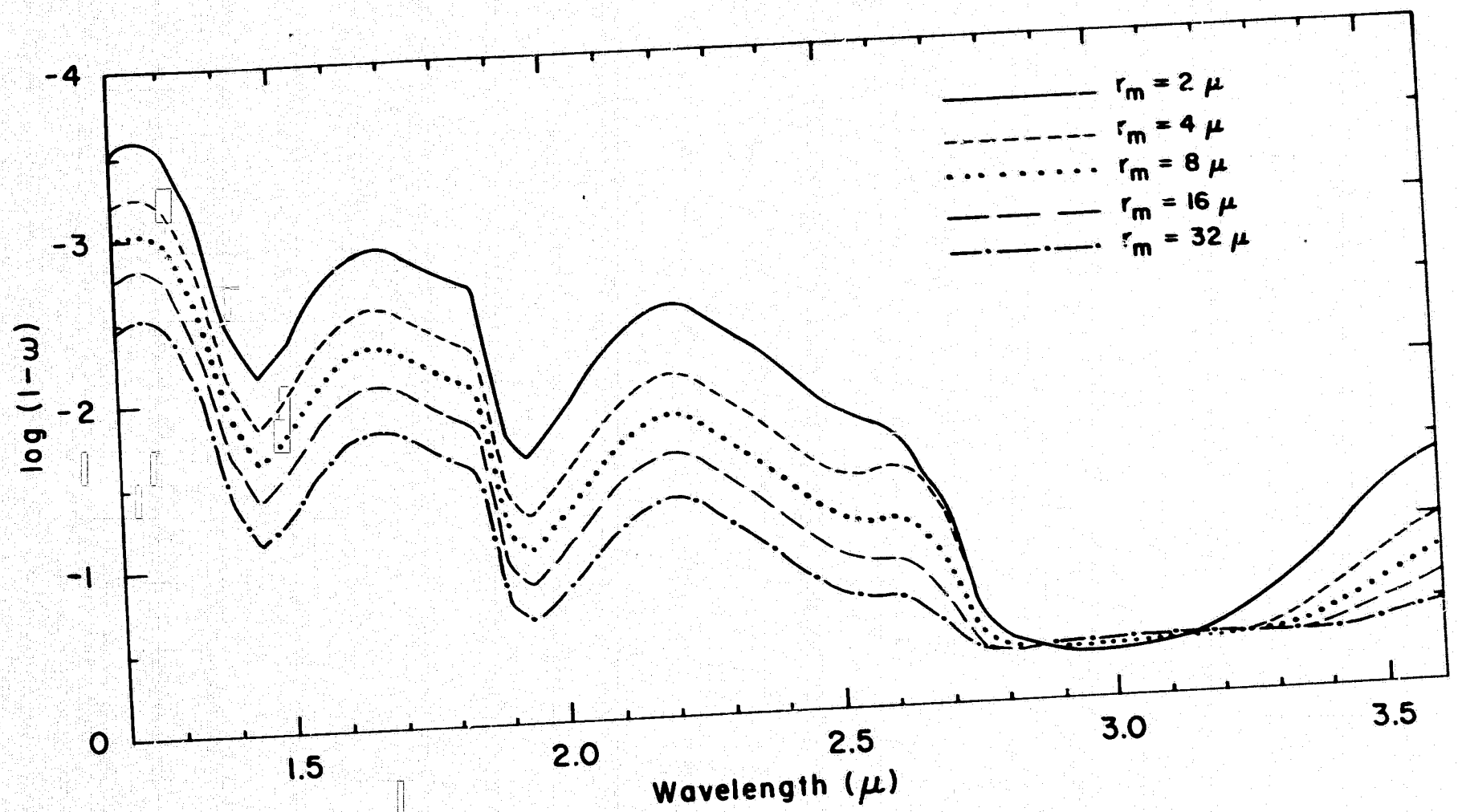
$r_m = 2\ \mu$
$r_m = 4\ \mu$
$r_m = 8\ \mu$
$r_m = 16\ \mu$
$r_m = 32\ \mu$
log (1 − ω)
-4
-3
-2
-1
0
1.5
2.0
2.5
3.0
3.5
Wavelength (μ)

Fig. 4

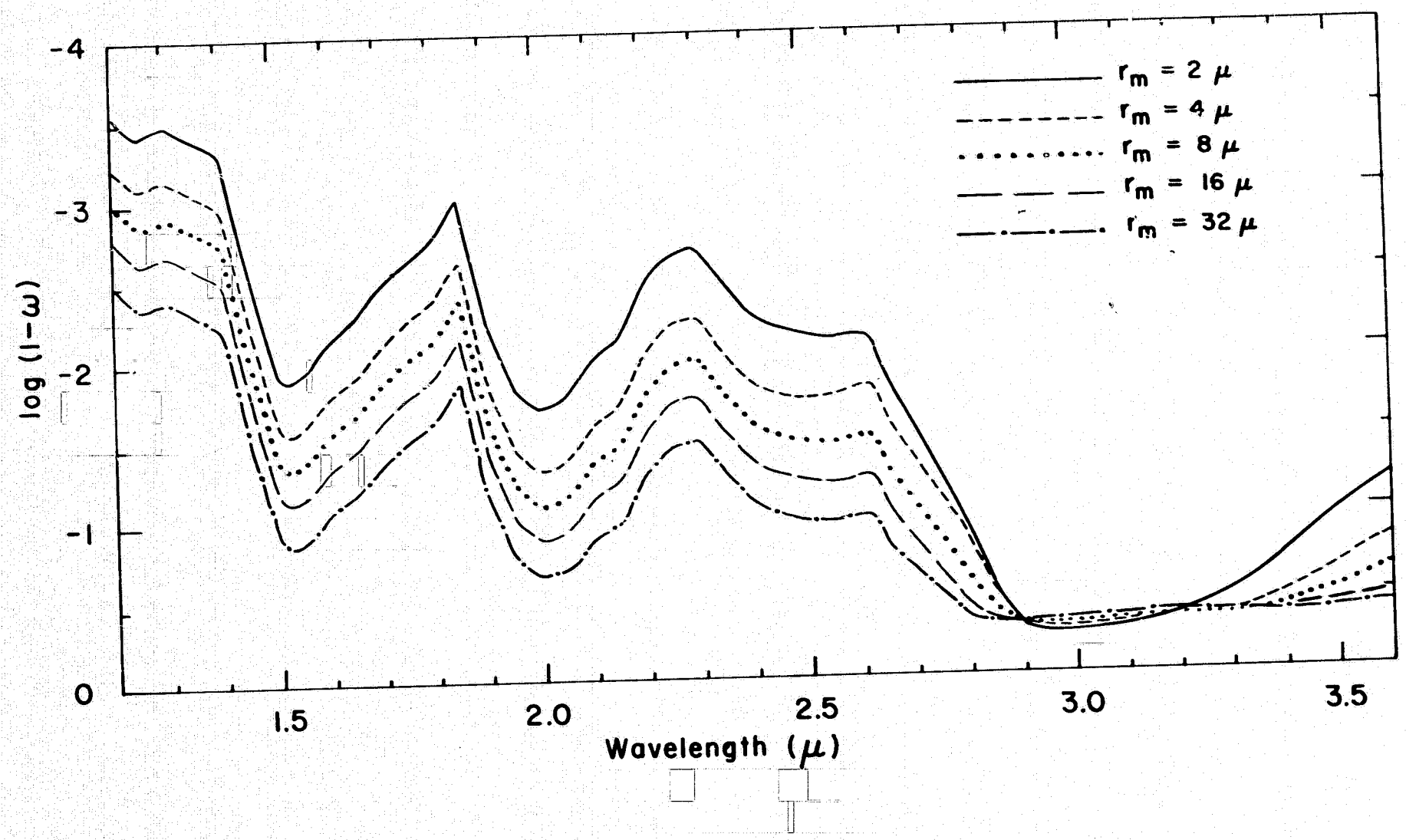
$r_m = 2\ \mu$
$r_m = 4\ \mu$
$r_m = 8\ \mu$
$r_m = 16\ \mu$
$r_m = 32\ \mu$
log (1−ω)
-4
-3
-2
-1
0
1.5
2.0
2.5
3.0
3.5
Wavelength (μ)

Fig. 5

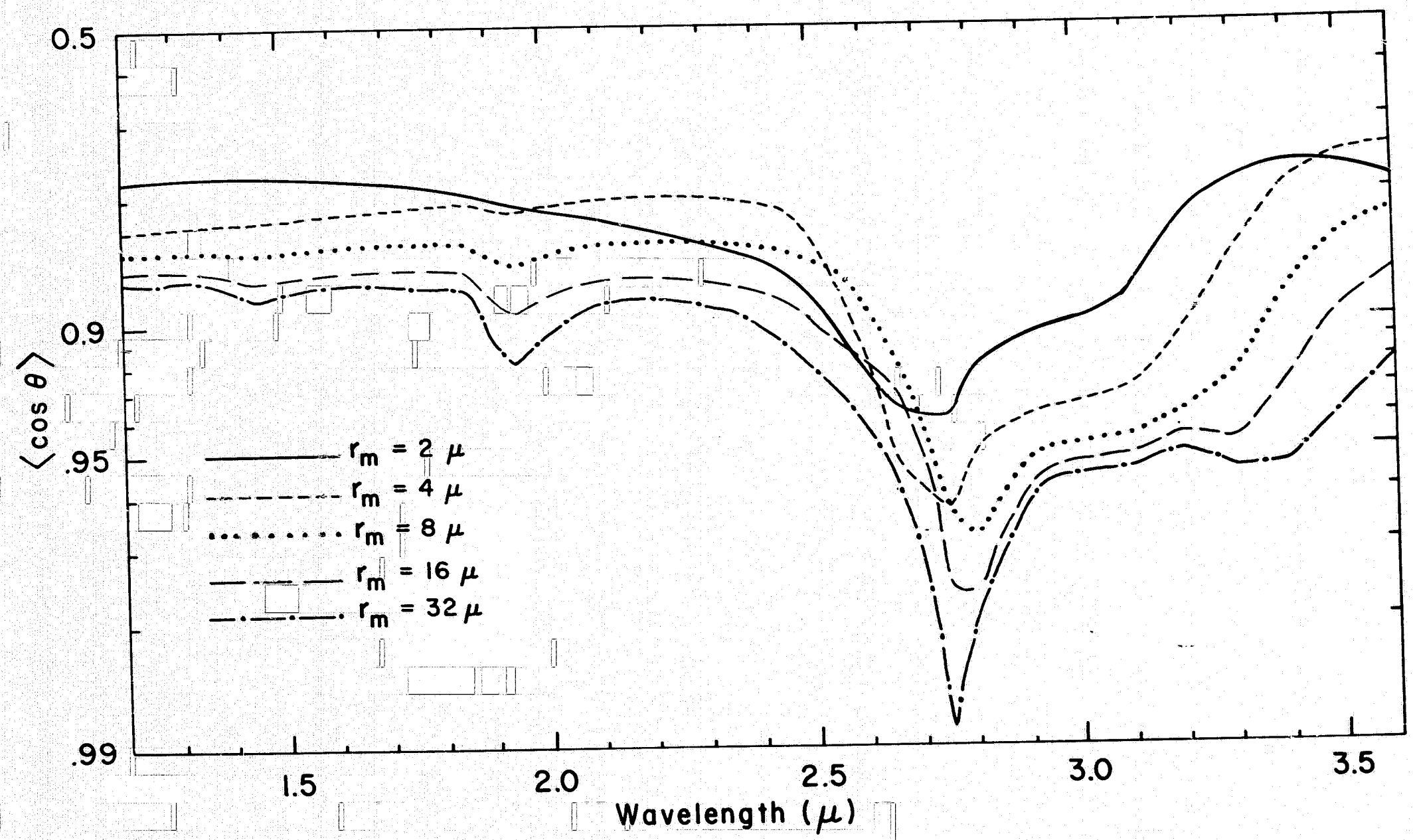
0.5
0.9
.95
.99
1.5
2.0
2.5
3.0
3.5
Wavelength (μ)
⟨cos θ⟩
r_m = 2 μ
r_m = 4 μ
r_m = 8 μ
r_m = 16 μ
r_m = 32 μ

Fig. 6

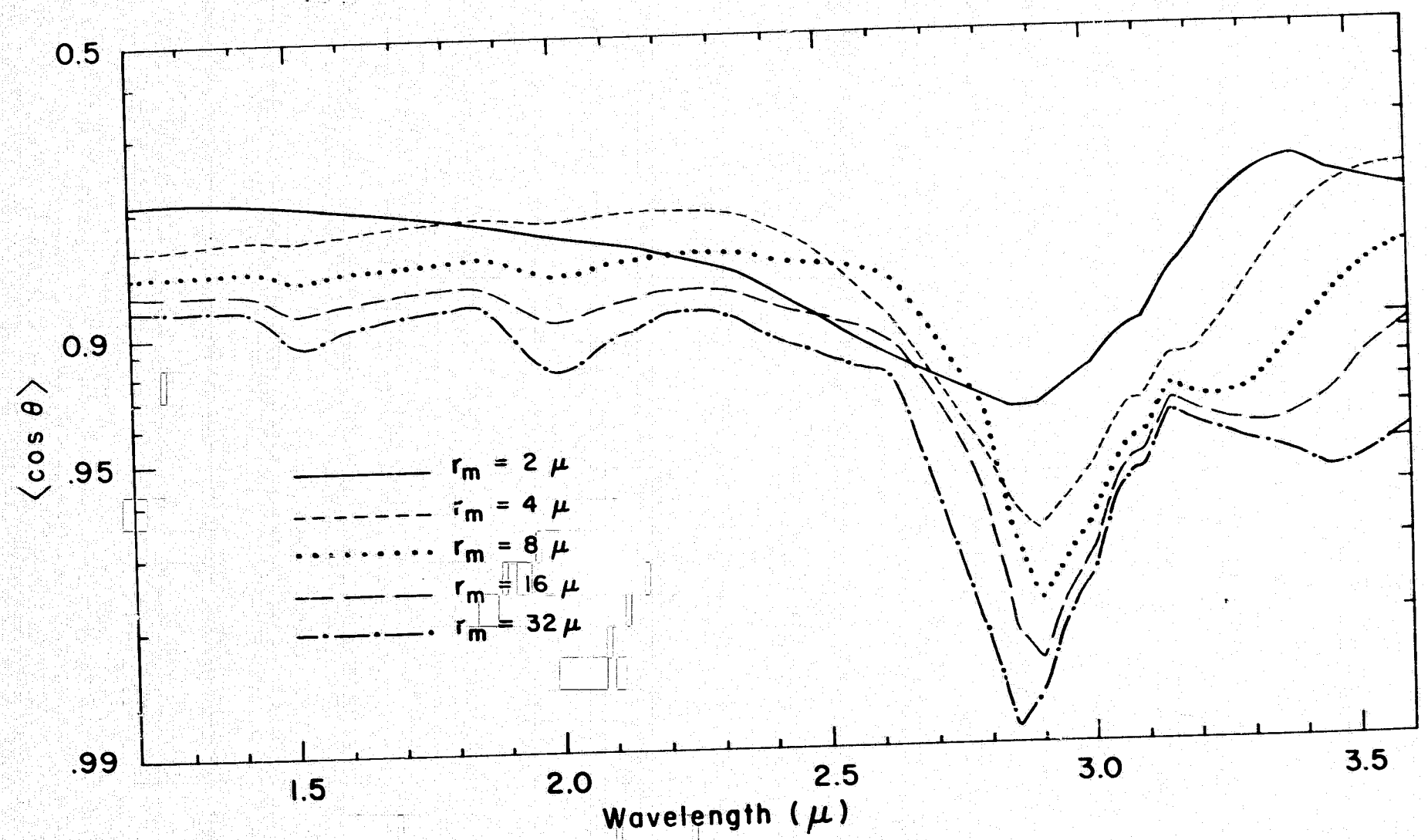
0.5
0.9
.95
.99
⟨cos θ⟩
1.5
2.0
2.5
3.0
3.5
Wavelength (μ)
r_m = 2 μ
r_m = 4 μ
r_m = 8 μ
r_m = 16 μ
r_m = 32 μ

Fig. 7

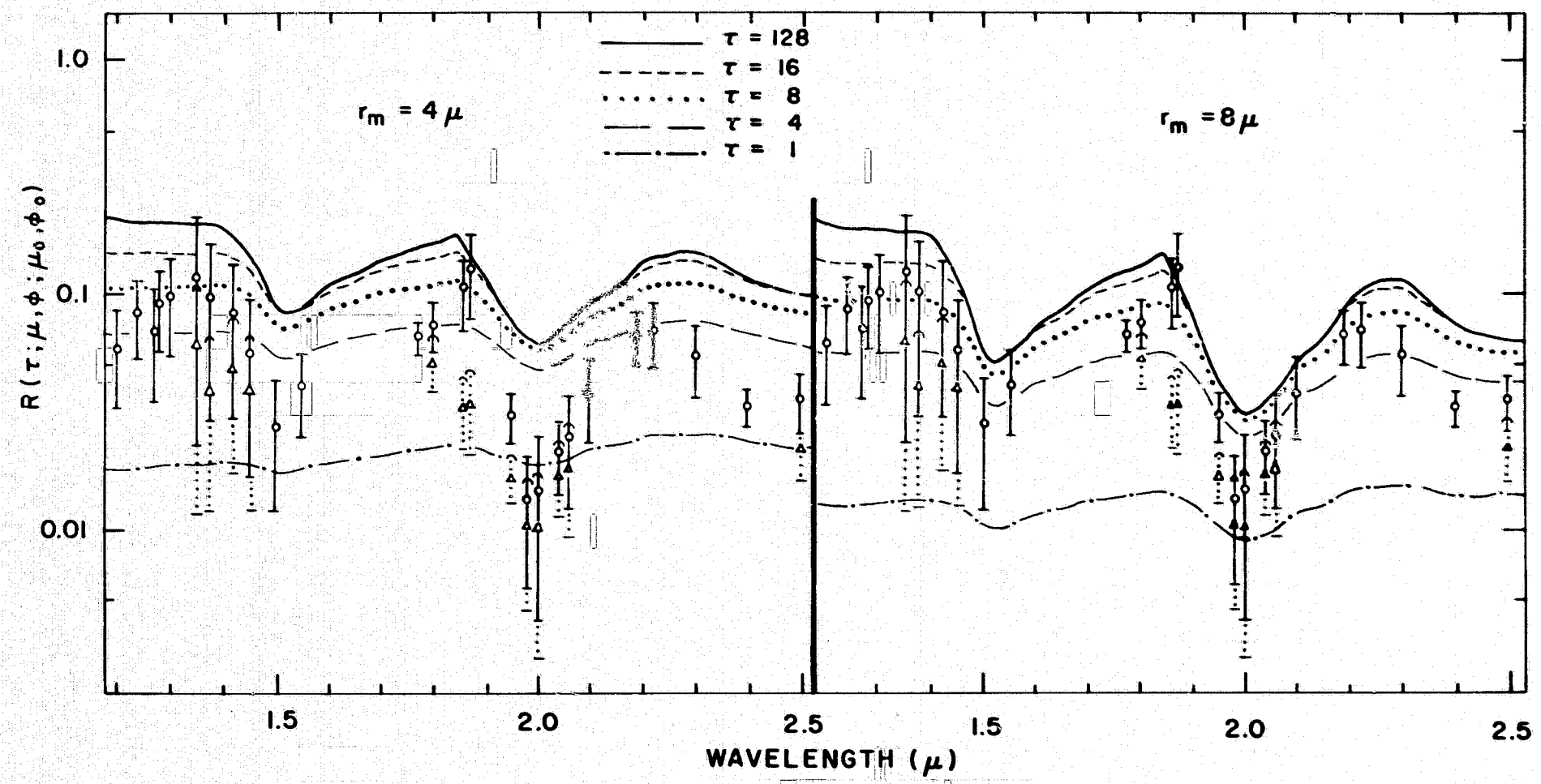
τ = 128
τ = 16
τ = 8
τ = 4
τ = 1
$r_m = 4\mu$
$r_m = 8\mu$
1.0
0.1
0.01
$R(\tau;\mu,\phi;\mu_0,\phi_0)$
1.5
2.0
2.5
1.5
2.0
2.5
WAVELENGTH (μ)

Fig. 8

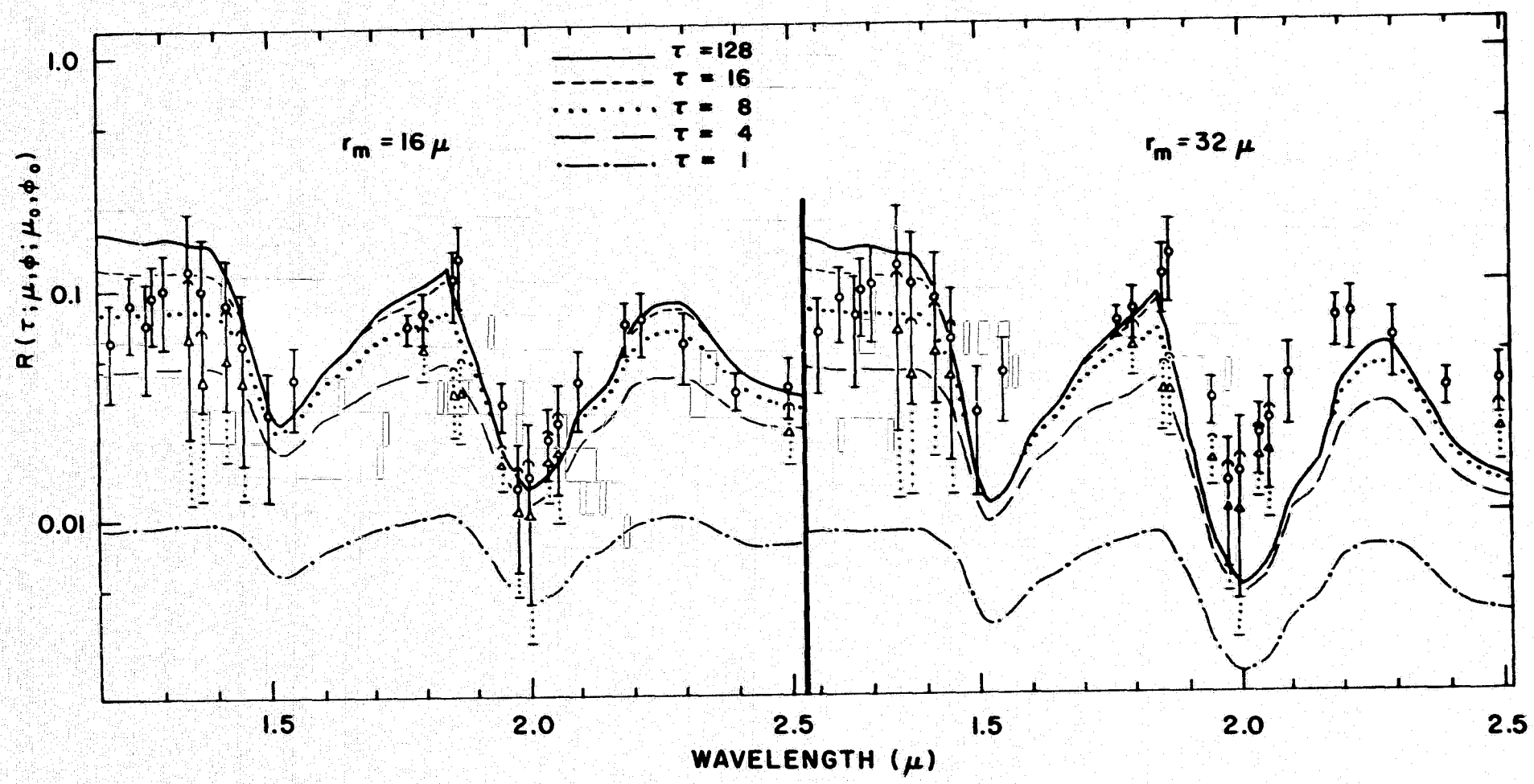
τ = 128
τ = 16
τ = 8
τ = 4
τ = 1
$r_m = 16\,\mu$
$r_m = 32\,\mu$
1.0
0.1
0.01
$R(\tau;\mu;\phi;\mu_0,\phi_0)$
1.5
2.0
2.5
1.5
2.0
2.5
WAVELENGTH (μ)

Fig. 9

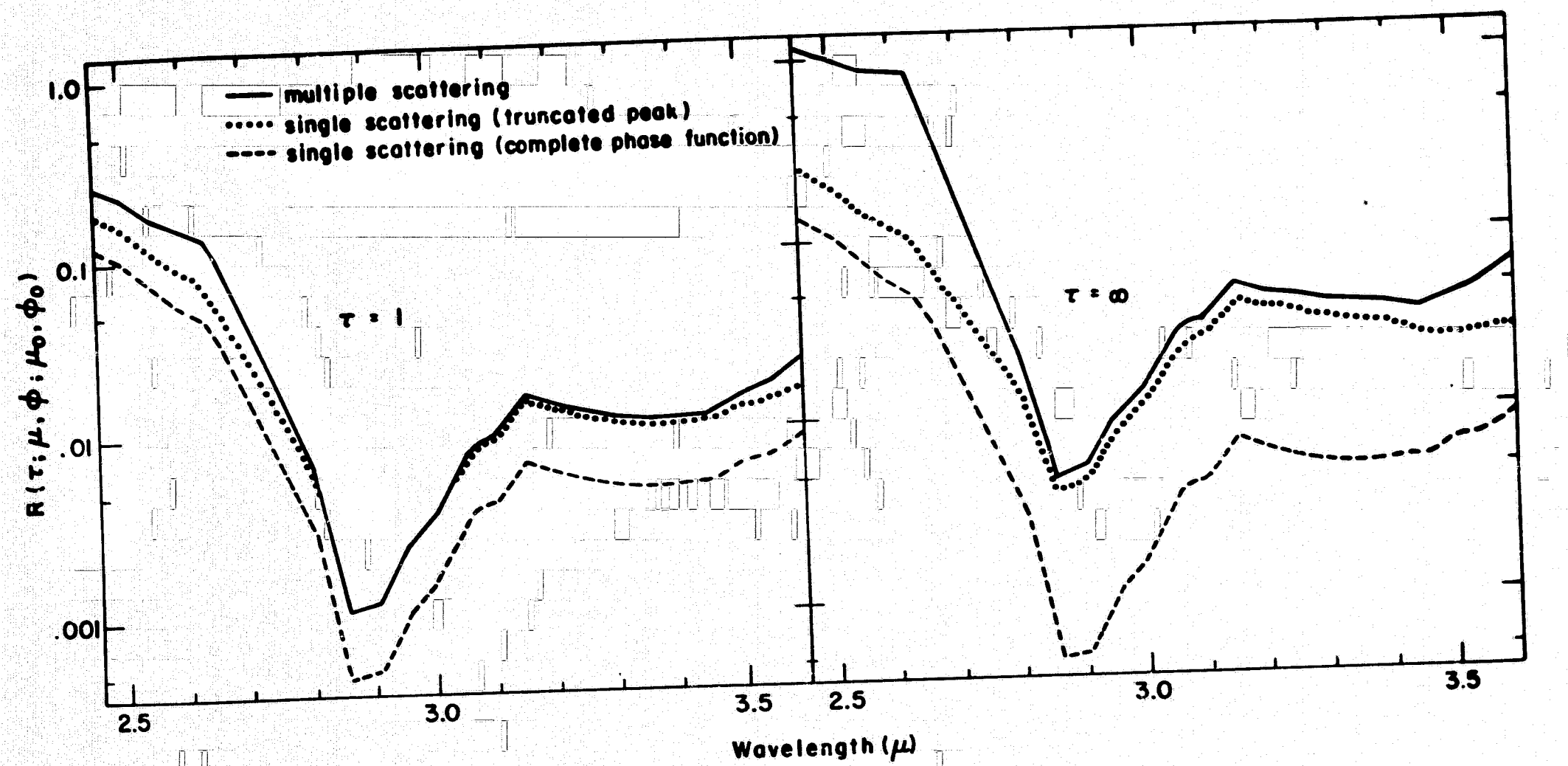
multiple scattering
single scattering (truncated peak)
single scattering (complete phase function)
$R(\tau;\mu,\phi;\mu_0,\phi_0)$
1.0
0.1
.01
.001
$\tau = 1$
$\tau = \infty$
2.5
3.0
3.5
Wavelength (μ)

Fig. 10

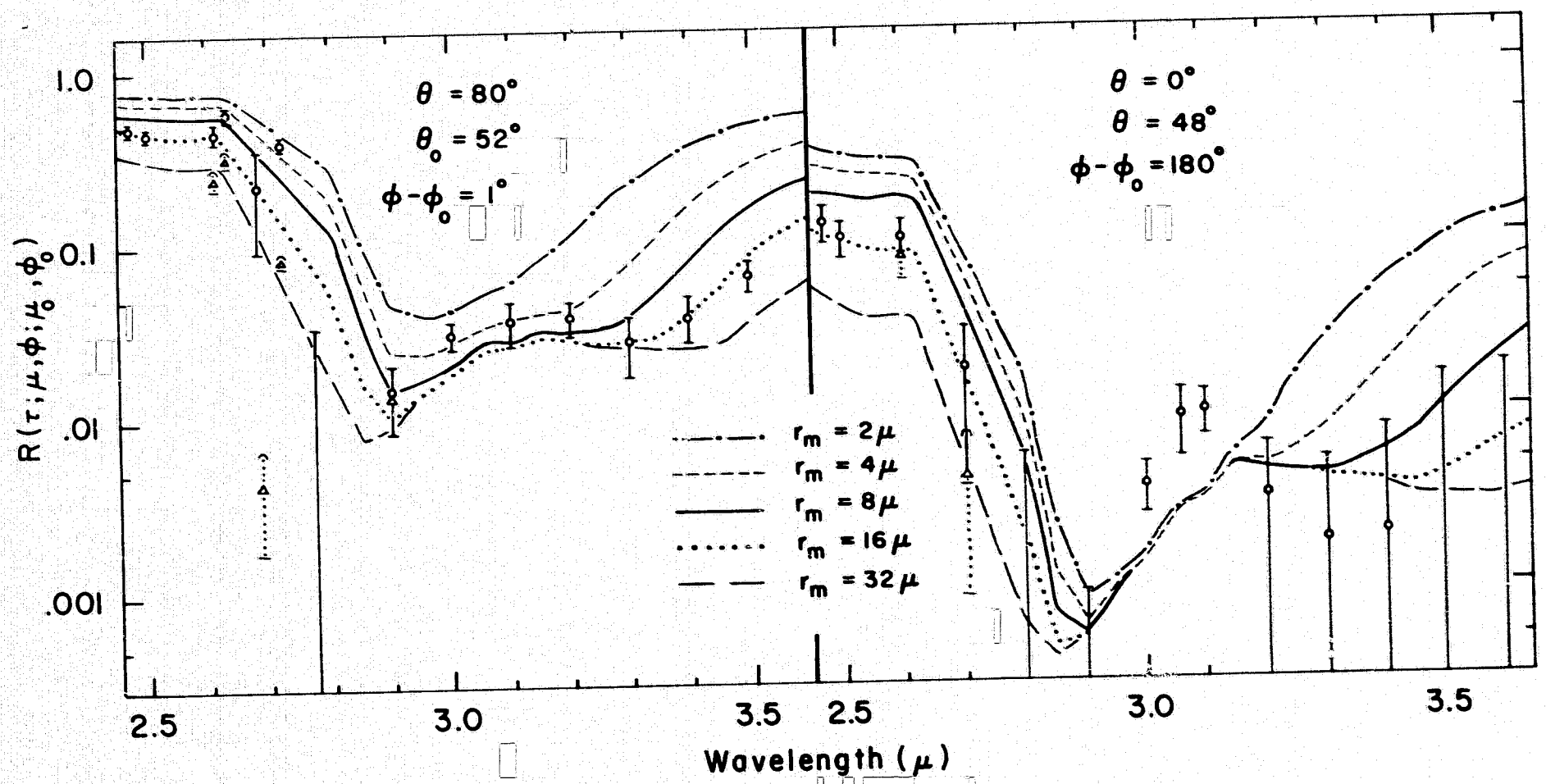
θ = 80°
θ₀ = 52°
φ-φ₀ = 1°
θ = 0°
θ = 48°
φ-φ₀ = 180°
r_m = 2μ
r_m = 4μ
r_m = 8μ
r_m = 16μ
r_m = 32μ
R(τ;μ,φ;μ₀,φ₀)
1.0
0.1
.01
.001
2.5
3.0
3.5
Wavelength (μ)

Fig. 11

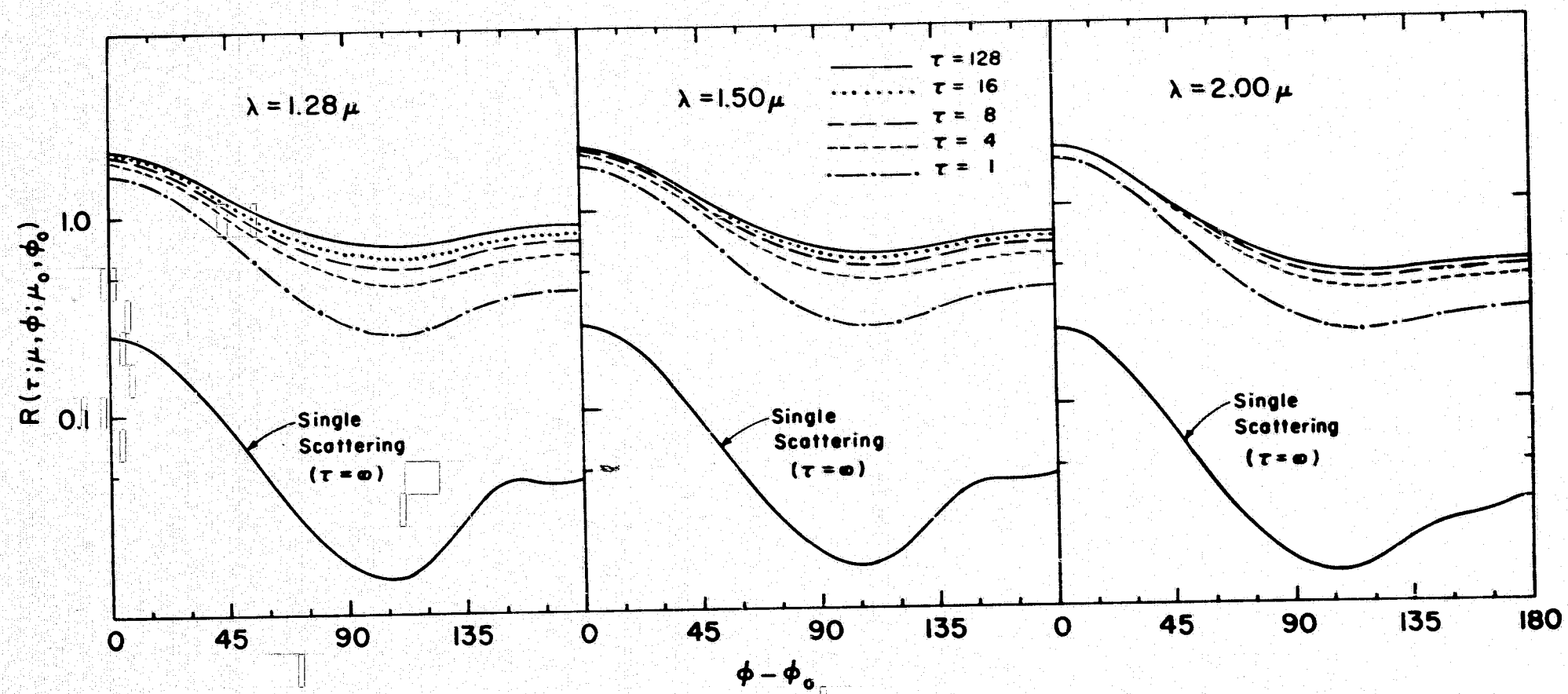
λ = 1.28 μ
λ = 1.50 μ
λ = 2.00 μ
τ = 128
τ = 16
τ = 8
τ = 4
τ = 1
Single Scattering (τ = ∞)
Single Scattering (τ = ∞)
Single Scattering (τ = ∞)
R(τ;μ,φ;μ₀,φ₀)
1.0
0.1
0
45
90
135
0
45
90
135
0
45
90
135
180
φ − φ₀

Fig. 12

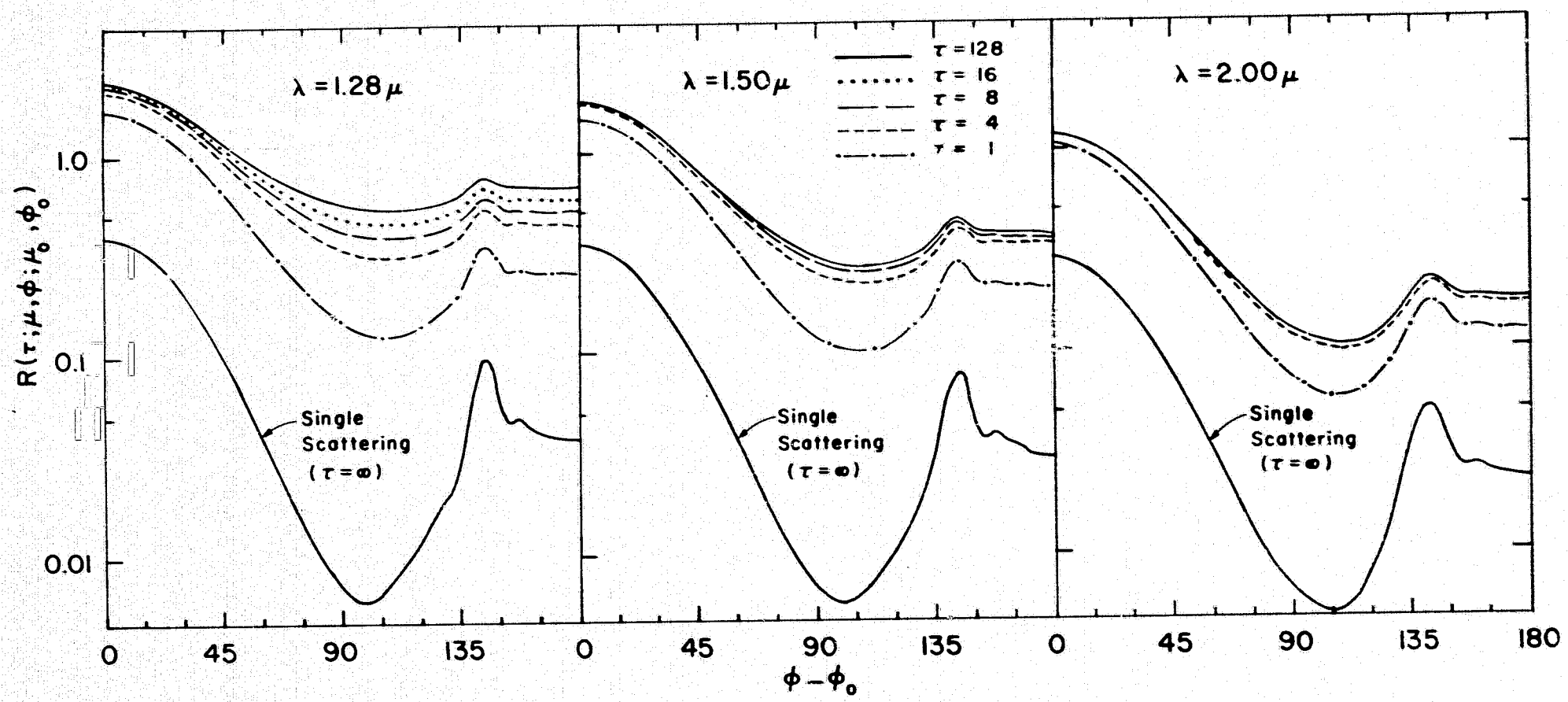
λ = 1.28 μ
λ = 1.50 μ
λ = 2.00 μ
τ = 128
τ = 16
τ = 8
τ = 4
τ = 1
1.0
0.1
0.01
R(τ;μ,φ;μ₀,φ₀)
Single Scattering (τ = ∞)
0
45
90
135
180
φ − φ₀

Fig. 13

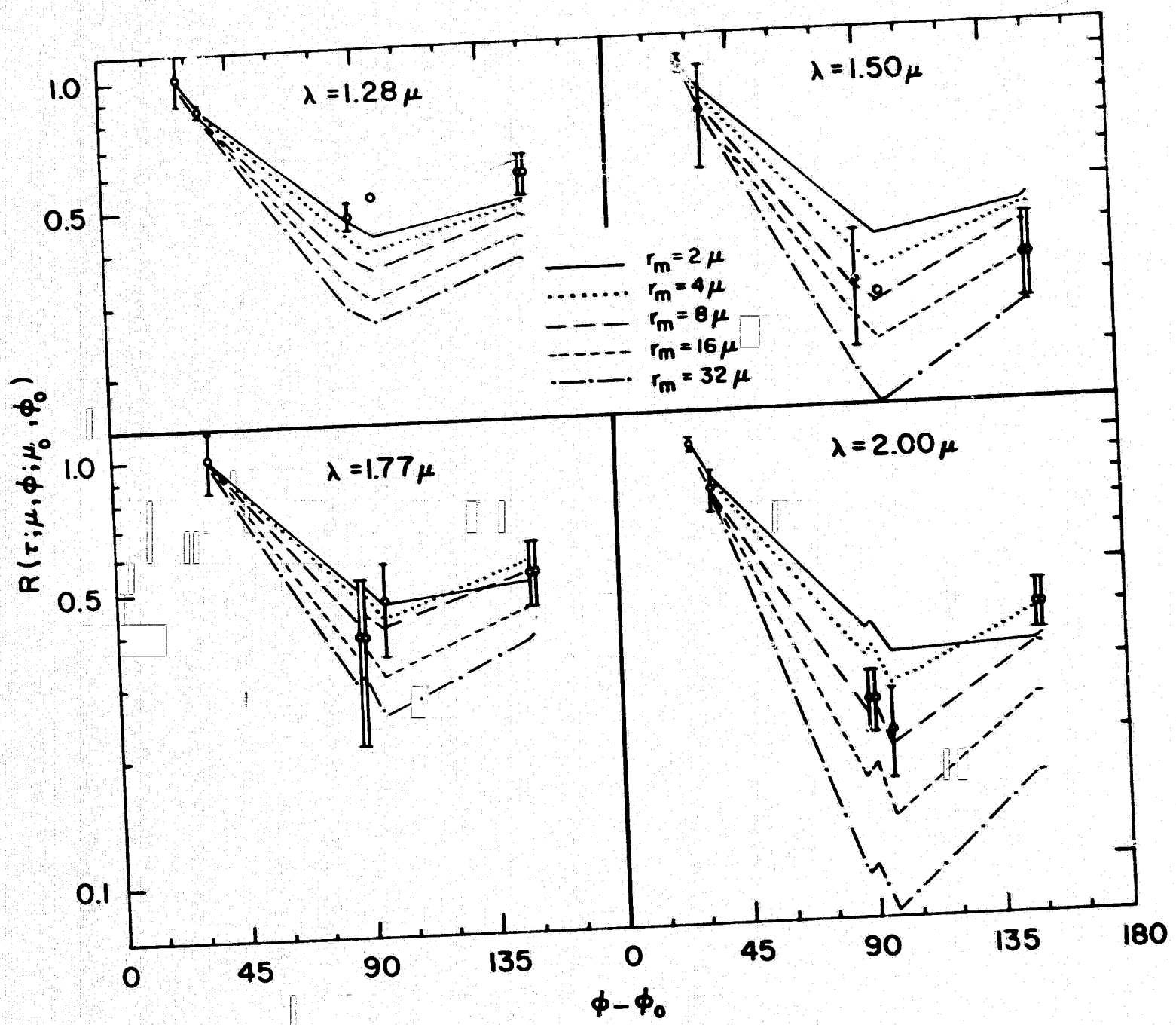
λ = 1.28 μ
λ = 1.50 μ
λ = 1.77 μ
λ = 2.00 μ
$r_m = 2\,\mu$
$r_m = 4\,\mu$
$r_m = 8\,\mu$
$r_m = 16\,\mu$
$r_m = 32\,\mu$
$R(\tau;\mu,\phi;\mu_0,\phi_0)$
1.0
0.5
0.1
0
45
90
135
180
$\phi - \phi_0$

Fig. 14

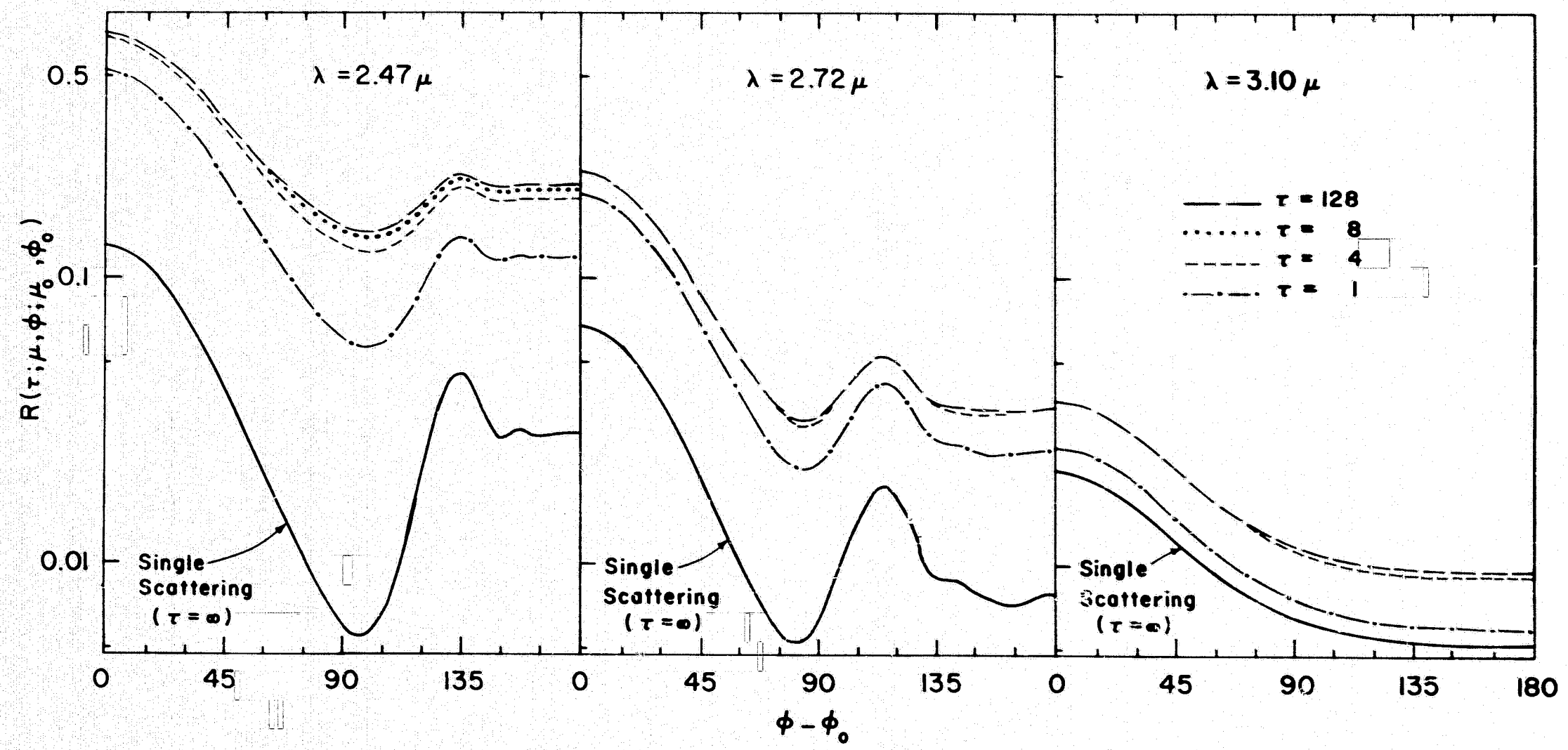
λ = 2.47 μ
λ = 2.72 μ
λ = 3.10 μ
τ = 128
τ = 8
τ = 4
τ = 1
Single Scattering (τ = ∞)
Single Scattering (τ = ∞)
Single Scattering (τ = ∞)
0.5
0.1
0.01
R(τ;μ,φ;μ₀,φ₀)
0
45
90
135
180
φ − φ₀

Fig. 15

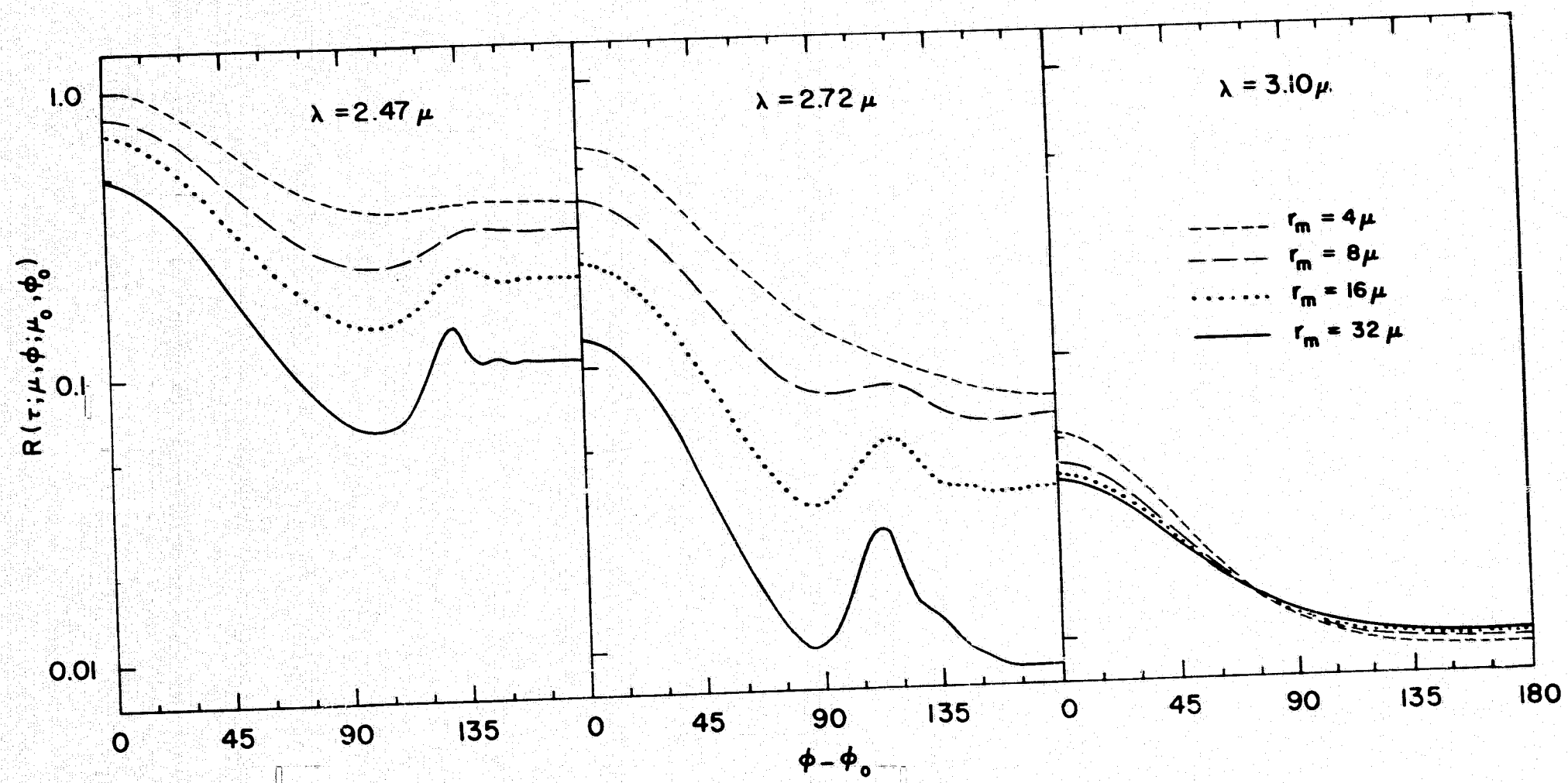
λ = 2.47 μ
λ = 2.72 μ
λ = 3.10 μ
r_m = 4 μ
r_m = 8 μ
r_m = 16 μ
r_m = 32 μ
1.0
0.1
0.01
R(τ;μ,φ;μ₀,φ₀)
0
45
90
135
180
φ − φ₀

Fig. 16

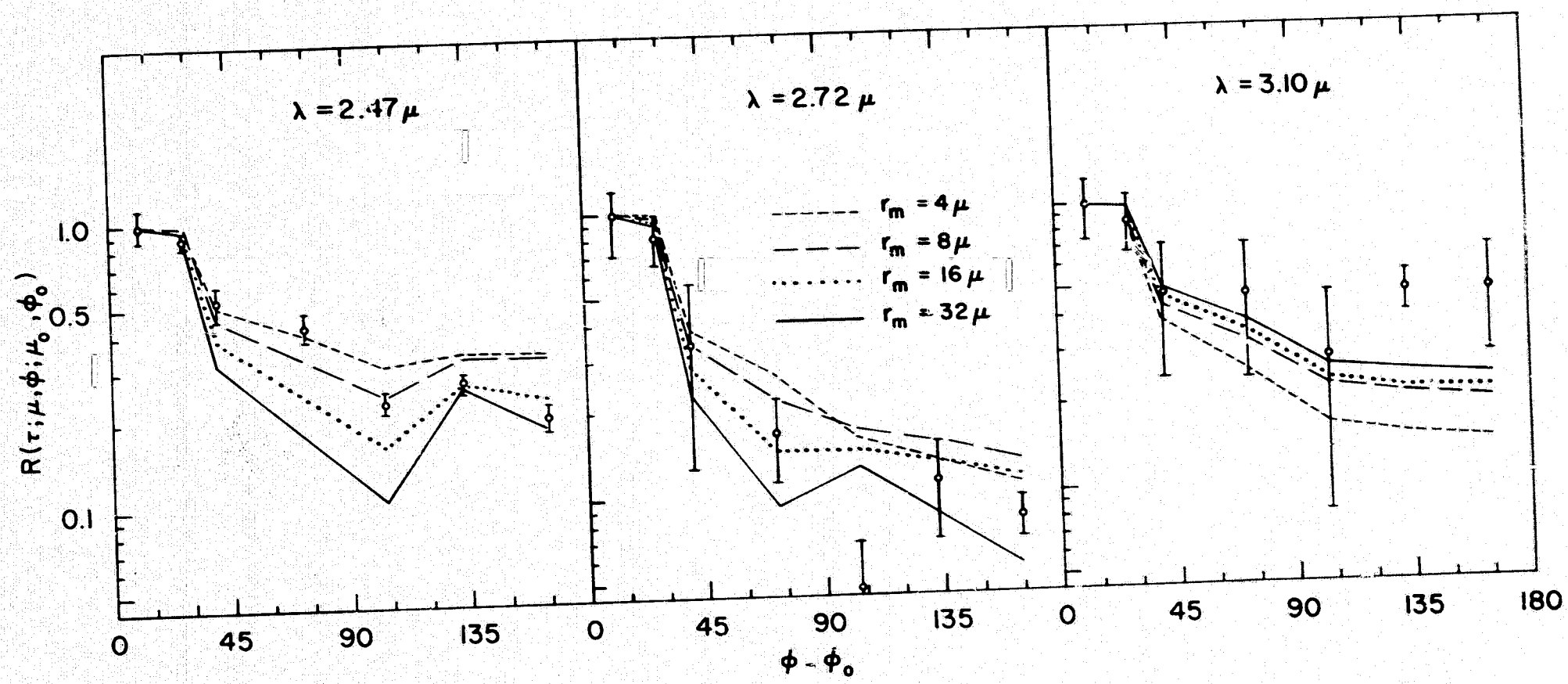
λ = 2.47 μ
λ = 2.72 μ
λ = 3.10 μ
r_m = 4 μ
r_m = 8 μ
r_m = 16 μ
r_m = 32 μ
R(τ;μ,φ;μ₀,φ₀)
1.0
0.5
0.1
0
45
90
135
180
φ - φ₀

Fig. 17

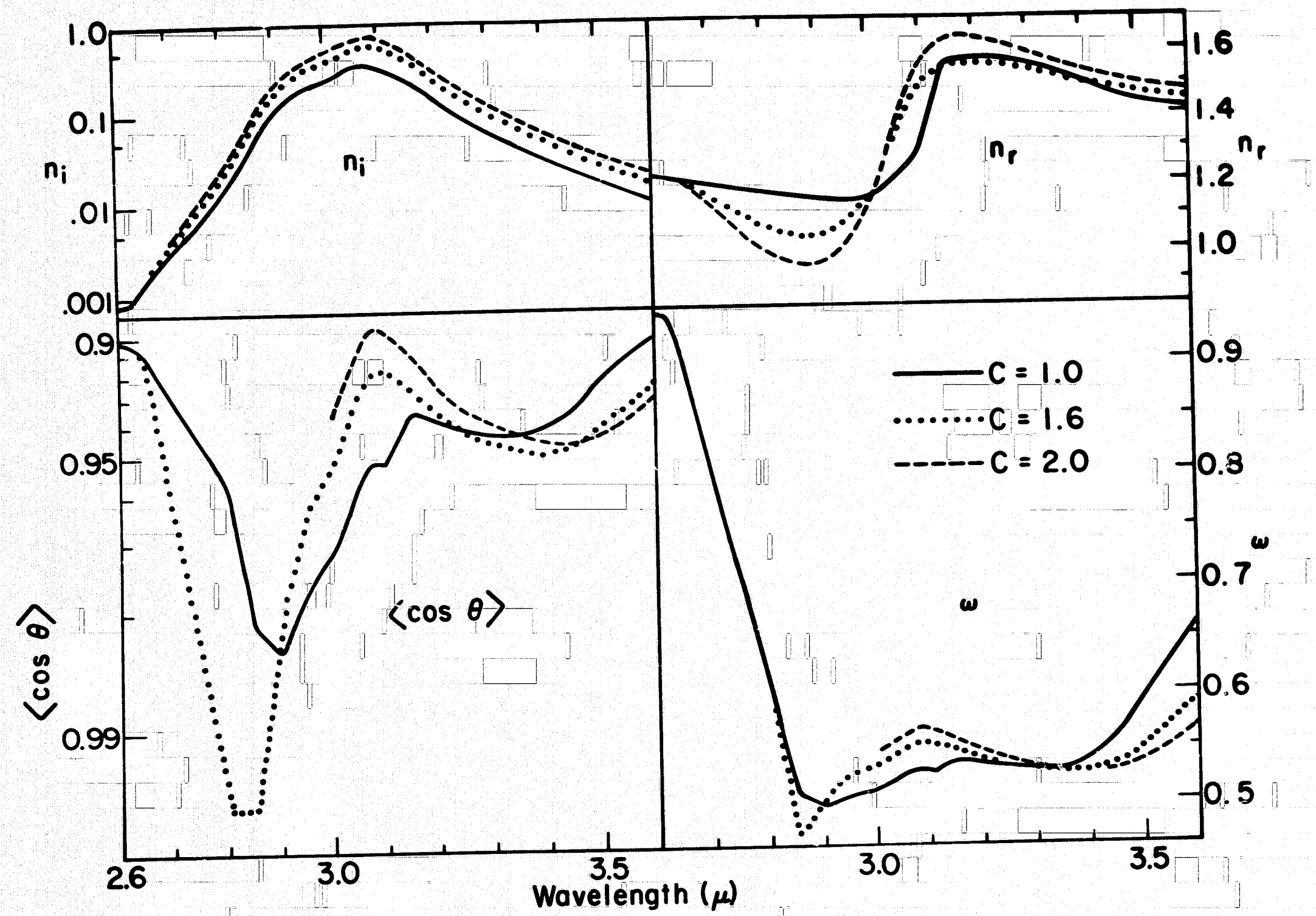
1.0
0.1
.01
.001
n_i
n_i
1.6
1.4
1.2
1.0
n_r
n_r
0.9
0.95
0.99
$\langle \cos\theta \rangle$
$\langle \cos\theta \rangle$
0.9
0.8
0.7
0.6
0.5
ω
ω
C = 1.0
C = 1.6
C = 2.0
2.6
3.0
3.5
3.0
3.5
Wavelength (μ)

Fig. 18

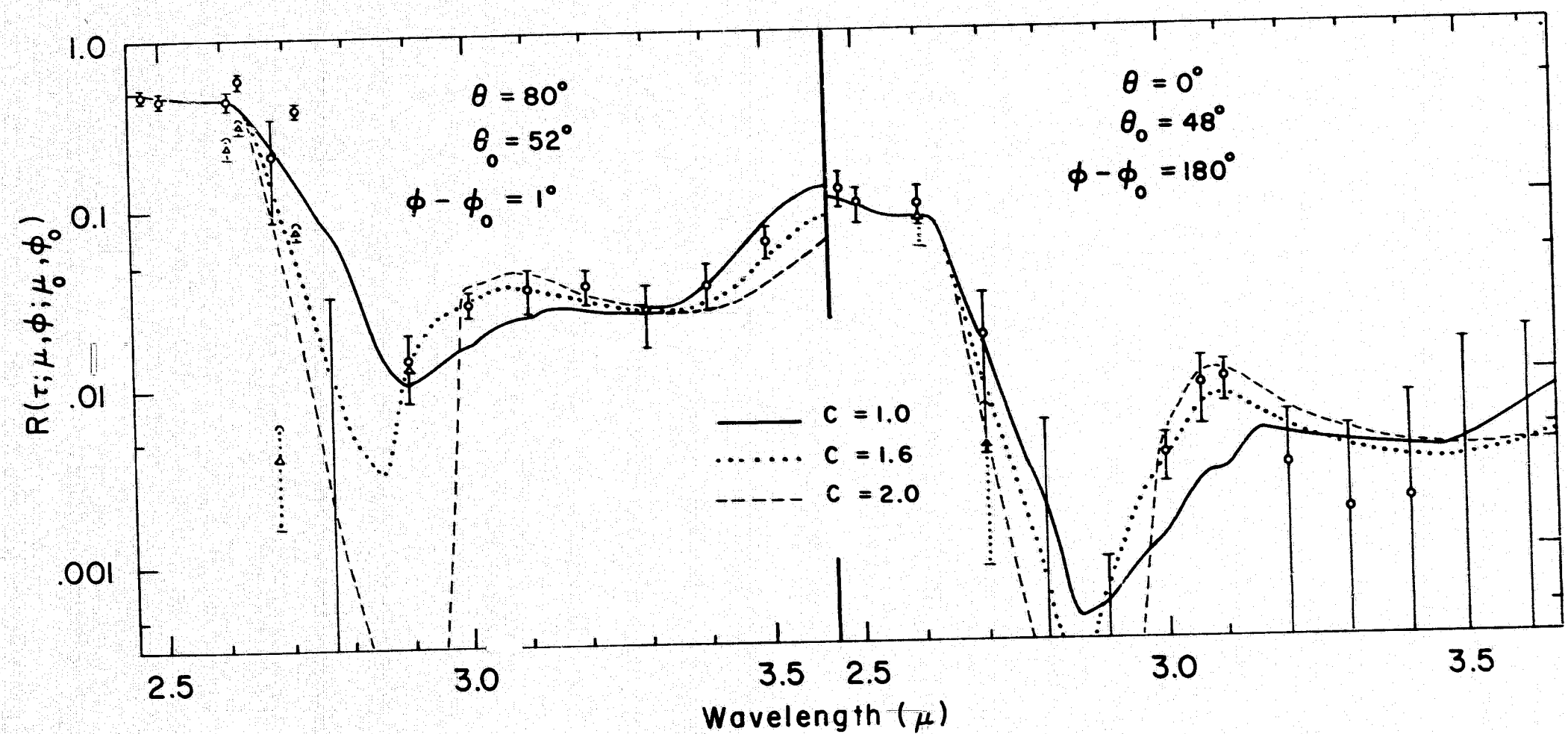
1.0
0.1
.01
.001
$R(\tau;\mu,\phi;\mu_0,\phi_0)$
$\theta = 80°$
$\theta_0 = 52°$
$\phi - \phi_0 = 1°$
$\theta = 0°$
$\theta_0 = 48°$
$\phi - \phi_0 = 180°$
C = 1.0
C = 1.6
C = 2.0
2.5
3.0
3.5
2.5
3.0
3.5
Wavelength (μ)

Fig. 19